Altering the threshold of an excitable signal transduction network changes cell migratory modes

Yuchuan Miao[1], Sayak Bhattacharya[2], Marc Edwards[3], Huaqing Cai[4], Takanari Inoue[3], Pablo A. Iglesias[2,3] and Peter N. Devreotes[3,5]

The diverse migratory modes displayed by different cell types are generally believed to be idiosyncratic. Here we show that the migratory behaviour of *Dictyostelium* was switched from amoeboid to keratocyte-like and oscillatory modes by synthetically decreasing phosphatidylinositol-4,5-bisphosphate levels or increasing Ras/Rap-related activities. The perturbations at these key nodes of an excitable signal transduction network initiated a causal chain of events: the threshold for network activation was lowered, the speed and range of propagating waves of signal transduction activity increased, actin-driven cellular protrusions expanded and, consequently, the cell migratory mode transitions ensued. Conversely, innately keratocyte-like and oscillatory cells were promptly converted to amoeboid by inhibition of Ras effectors with restoration of directed migration. We use computational analysis to explain how thresholds control cell migration and discuss the architecture of the signal transduction network that gives rise to excitability.

Diverse cells display different migratory modes. For example, amoeba move by repeatedly extending and retracting pseudopods, keratocytes glide with a single broad anterior protrusion, fibroblasts slowly project filopodia and lamellipodia with strong attachment, and some cells display oscillatory behaviour[1–6]. Transitions between these migratory behaviours can be important, for example as cancer cells become metastatic[7,8]. While these migratory modes probably depend on a constellation of expressed genes, the connections among different genetic profiles, various types of protrusion, and cell migratory modes are not understood.

In amoeboid cells, random migration requires activation of the same signal transduction networks that are triggered by extracellular cues[9–11]. These networks contain multiple compensatory pathways involving Ras superfamily GTPases, phosphoinositides and kinases and phosphatases[12–15]. Coordinated increases or decreases in these activities start spontaneously and propagate in waves along the cell cortex that are spatiotemporally correlated with actin waves, which are thought to drive pseudopodia formation at the edge of the cell[11,16–26]. Thus, an understanding of the relationship among waves of signal transduction activities, cytoskeletal events and cellular protrusions may reveal the essential differences between distinct migratory modes.

We have proposed that the signal transduction components involved in cell migration are linked in a signal transduction excitable network (STEN). In addition to wave propagation, evidence for excitability includes all-or-none responses to supra-threshold stimuli and the existence of a refractory period[11,17]. In the classical example of the action potential, excitability derives from self-amplifying positive and delayed negative feedback loops comprised of voltage-gated ion channels, whereas in cell migration these loops most likely involve biochemical interactions. Computational models based on excitability have led to realistic simulations of random and directed cell migration[11,16,27–32]. These models suggest that small changes in thresholds can alter wave properties and lead to distinct patterns of behaviour, but this has not been experimentally tested.

Here, we hypothesize that the spectrum of cell migratory modes observed in various cells arises from the different set points, or thresholds, of STEN. Since components in the STEN undergo highly coordinated transient changes during network activation, 'clamping' one component near the level it achieves during activation (or inactivation) might alter the excitability of the entire network, offering an excellent opportunity to test the idea.

RESULTS

Acute perturbations of STEN components control migratory profiles

We used a chemically inducible dimerization system in *Dictyostelium* to clamp phosphatidylinositol-4,5-bisphosphate (PtdIns(4,5)P$_2$) at low levels or the activities of Ras/Rap GTPases at high levels, as

[1]Department of Biological Chemistry, School of Medicine, Johns Hopkins University, Baltimore, Maryland 21205, USA. [2]Department of Electrical and Computer Engineering, Whiting School of Engineering, Johns Hopkins University, Baltimore, Maryland 21205, USA. [3]Department of Cell Biology and Center for Cell Dynamics, School of Medicine, Johns Hopkins University, Baltimore, Maryland 21205, USA. [4]State Key Laboratory of Biomacromolecules, Institute of Biophysics, Chinese Academy of Sciences, Beijing 100101, China.
[5]Correspondence should be addressed to P.N.D. (e-mail: pnd@jhmi.edu)

329
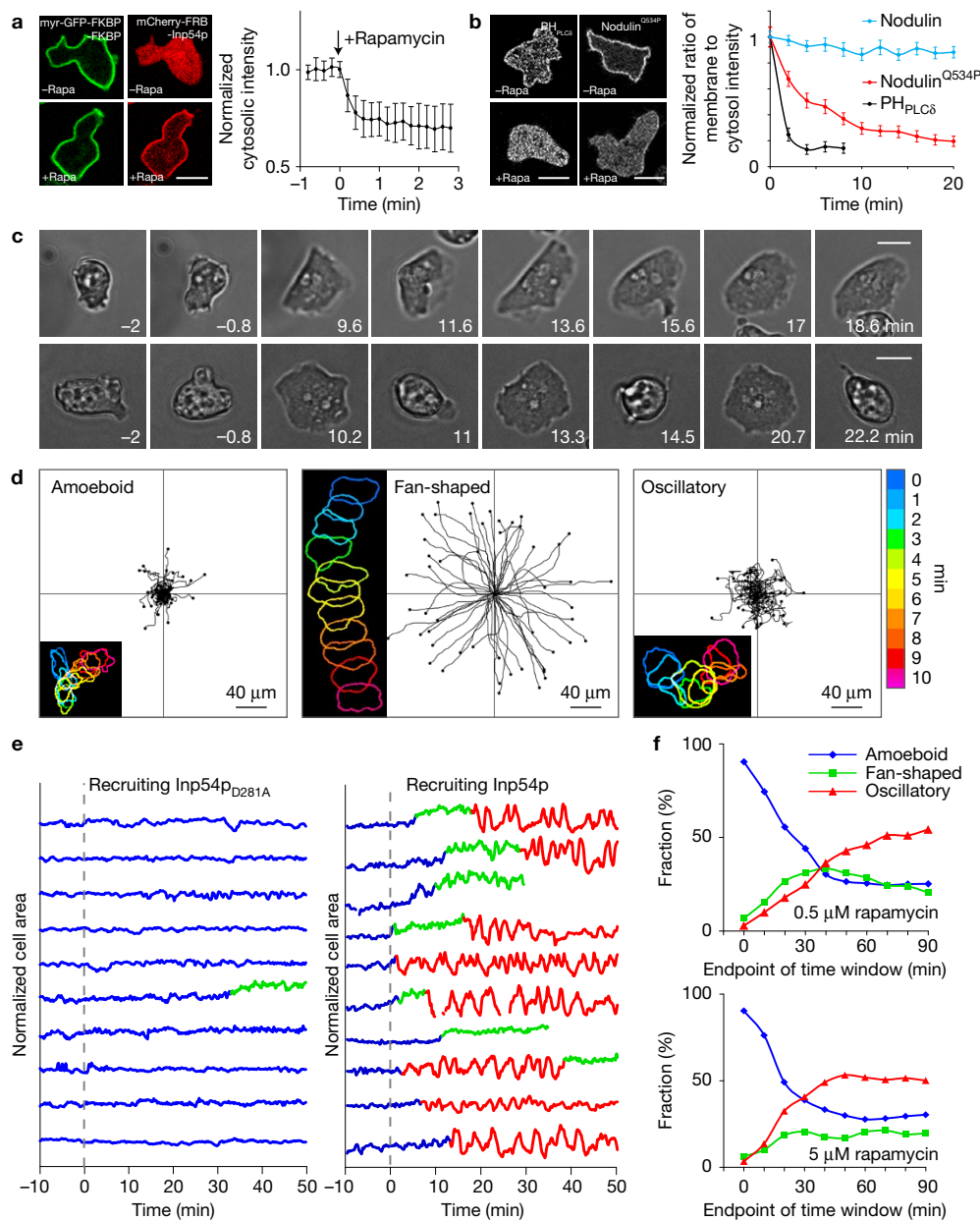
Figure 1 Acute clamping of PtdIns(4,5)P$_2$ at lowered levels triggers cell migratory mode transitions. (**a**) Left, confocal images of myr-GFP-FKBP-FKBP (green) and mCherry-FRB-Inp54p (red) before and after rapamycin treatment. Right, temporal profile of normalized intensity of cytosolic mCherry (mean ± s.d., $n = 25$ cells). (**b**) Left, confocal images of PtdIns(4,5)P$_2$ biosensors PH$_{PLC\delta}$-YFP and GFP-nodulin^{Q534P} before and after rapamycin treatment. Right, normalized ratios of membrane to cytosol intensity of PH$_{PLC\delta}$-YFP (black), GFP-nodulin^{Q534P} (red) and GFP-nodulin (blue) following rapamycin treatment at time 0 (mean ± s.e.m., $n = 21$ cells for each biosensor). Initial data are shown in Supplementary Fig. 1a. ('Nodulin' refers to the Nlj6-like nodulin domain of the *Arabidopsis* Sec14-nodulin protein AtSfh1 (ref. 41); nodulin^{Q534P} is a mutant with defects in self-oligomerization and thus diminished affinity for PtdIns(4,5)P$_2$ compared with nodulin.) (**c**) Time-lapse phase-contrast images showing the transition of an amoeboid cell to a fan-shaped (top) or an oscillatory cell (bottom). Scale bars in all images represent 10 μm. (**d**) Centroid tracks showing random movement of amoeboid (left), fan-shaped (middle) and oscillatory (right) cells. Each track lasts 10 min and was reset to the same origin. Insets show colour-coded (1-min intervals) outlines of a cell. Velocity (μm min^{-1}) and directedness are 4.2 ± 1.6 and 0.39 for amoeboid, 11.7 ± 1.8 and 0.91 for fan-shaped, and 7.5 ± 2.0 and 0.40 for oscillatory cells (mean ± s.d., $n = 50$ cells for each). (**e**) Temporal profiles of normalized areas of 10 control (left) and experimental cells (right). The dashed lines indicate the addition of rapamycin at time 0. Based on the corresponding videos, amoeboid, fan-shaped and oscillatory modes are coloured as blue, green and red respectively. (**f**) Fractions of each migratory mode in 10-min time windows in a cell population of ∼100 cells before and after Inp54p recruitment. 0.5 μM (top) or 5 μM (bottom) rapamycin was added at time 0.

would be expected to transiently occur during STEN activation[33–38]. To decrease PtdIns(4,5)P$_2$, we co-expressed myristoylated FKBP and the yeast PtdIns(4,5)P$_2$-specific phosphatase Inp54p[39,40] fused to FRB. Following addition of rapamycin, mCherry-FRB-Inp54p

was rapidly and irreversibly recruited to the plasma membrane (Fig. 1a). Several PtdIns(4,5)P$_2$ biosensors with different apparent affinities, including PH$_{PLC\delta}$ and derivatives of nodulin[41], suggested that PtdIns(4,5)P$_2$ levels decreased rapidly, reaching a new lower

steady-state level within 15 min (Fig. 1b and Supplementary Fig. 1a). After rapamycin addition, the speed of the cell population increased to 7.3 ± 2.7 from 4.2 ± 2.0 μm min^{-1}, but not when inactive Inp54p$_{D281A}$ was recruited (Supplementary Fig. 1b,c and Supplementary Video 1). Similar increases in motility occurred when we recruited RasC$_{Q62L(\Delta CAAX)}$, Rap1$_{G12V(\Delta CAAX)}$, or the GEF domain of Rap1 GEF, GbpD[42] (Supplementary Fig. 1d–f).

Careful examination revealed that initially amoeboid cells switched to fan-like or oscillatory behaviour (Fig. 1c and Supplementary Figs 2 and 3 and Supplementary Video 2). 'Fans' resemble gliding kerato-cytes, with broad protrusions along a wide anterior zone and a flat contractile back. 'Oscillators' spread globally, contracted strongly, and migrated briefly before repeating the cycle. The appearance of these distinct populations could also be detected with computer algorithms that defined fans, or oscillators, as cells that either migrated perpendic-ular to their long axis or displayed a large variance in area, respectively (Supplementary Fig. 4). The speed and directedness were much higher in the fan-shaped than in the amoeboid cells (Fig. 1d). The oscillatory cells were also faster than the amoeboid since they often glided into the spreading phase. The heterogeneity within the population is illustrated in Fig. 1e. Some cells transitioned persistently to fans or oscillators while others switched between modes. Retrospective examination of wild-type cells revealed that about 1% of cells displayed fan-like or oscillatory behaviours, but this increased to ∼10% when expressing cytosolic Inp54p. Following recruitment, the probability of the fan-shaped and oscillatory modes grew to about 20% and 50% respectively during 40 min (Fig. 1f). At a lower dose of rapamycin, fans were more prominent than oscillators at early time points but the same final distribution was reached (Fig. 1f), suggesting that the fan-shaped cells represent an intermediate phenotype.

We used LimE$_{\Delta coil}$-YFP (LimE) to monitor actin polymerization. Three-dimensional (3D) kymographs, or T-stacks, showed that newly polymerized F-actin was initially confined to patches but was localized in broad zones after the addition of rapamycin (Fig. 2a and Sup-plementary Video 3). Time-lapse videos revealed the spatiotemporal F-actin dynamics in different modes of migration (Fig. 2b,d,f and Supplementary Video 4). In kymographs of the amoeboid cells, narrow regions of LimE intensity appeared stochastically with low coordina-tion (Fig. 2c). In fans, broad, sometimes V-shaped, regions centred in the direction of migration appeared periodically, rarely extending to the back of the cell (Fig. 2e). In oscillators, LimE intensity was highly coordinated with cell area, increasing and decreasing during the spreading and contracting phases respectively (Fig. 2g,h). LimE usu-ally occupies 10–40% of the cell periphery in amoeboid cells, 40–70% in fans, and a broad range including 0 and 100% in oscillators (Fig. 2i). None of these intensity patterns was observed when we monitored cell periphery using recruited mCherry-FRB-Inp54p (Supplementary Fig. 5a–d). Similar LimE patterns were observed in cells after recruit-ing RasC$_{Q62L(\Delta CAAX)}$, Rap1$_{G12V(\Delta CAAX)}$, and GbpD-GEF (Supplemen-tary Video 5). These observations suggest that the lateral dimension of actin-filled projections plays a key role in cell migratory behaviour.

STEN activities are required for the transition in migratory modes

We examined whether activation of the STEN coincided with the large protrusions in fans and oscillators. As representatives of STEN activity, we used RBD-YFP, PH$_{crac}$-YFP and PTEN-GFP.

RBD, which monitors multiple Ras activities, and PH$_{crac}$, which reports phosphatidylinositol-(3,4,5)-trisphosphate (PtdIns(3,4,5)P$_3$) levels, are found preferentially at the front of migrating cells, at the tips of newly projected protrusions, in the active zones of propagating waves, and associate transiently with the plasma membrane during global stimulation. PTEN displays complementary localization and kinetics. In oscillatory cells, the 'front' biosensors were recruited to the membrane globally during the spreading phase and returned to the cytosol when the cell contracted whereas the 'back' marker, PTEN, moved oppositely (Fig. 3a–c and Supplementary Fig. 5e–g and Supplementary Video 6). In migrating fans RBD and PH$_{crac}$ were recruited to the front while PTEN located at the rear (Fig. 3a–c).

Next we sought to determine the extent to which the transition among migratory modes depended on changes in gene expression or STEN activities. Addition of 1 mg ml^{-1} cycloheximide did not block the induced migratory mode transitions (Supplementary Video 7). Previous studies have shown that heterotrimeric G proteins activate Ras and Rap small GTPases, leading to the activation of PI(3)K and TORC2, which converge on the activities of PKBs to organize actin polymerization. Here, loss of PKBA and PKBR1 ($pkbA^-/pkbR1^-$) blocked the induced mode transitions (Fig. 3d). Inhibition of neither PI(3)K nor TORC2 activities was sufficient to block the transitions, but combined inhibition with LY294002 plus PP242, or by LY294002 treatment of cells lacking the TORC2 subunit PiaA, nearly prevented the formation of fans and oscillators. Interference with small GTPases by expressing dominant-negative Rap1 (^{DN}Rap1), or double deletion of RasC and RasG ($rasC^-/rasG^-$), diminished the transitions, and combined perturbations blocked the responses. G-protein function was not required since Gγ deletion did not prevent the induced transitions. These suggest that the same STEN activities involved in chemoattractant stimulation are required for the enlarged protrusions underlying fans and oscillators.

Given that PKBs link the activity of the STEN to the cytoskeletal network, it is not surprising that they are required for the mode transitions, but these kinases have also been reported to negatively regulate RasC[36]. To access the effects of PKBs without interference of the cytoskeleton, we treated cells with latrunculin A to inhibit actin polymerization and monitored the activity of Ras and PI(3)K directly, using RBD and PH$_{crac}$. Cells lacking PKBs ($pkbA^-/pkbR1^-$) showed enhanced activities of both biosensors, which were suppressed by expressing PKBA (Fig. 3e). Similarly, elevated RBD activities were observed when LY294002 and PP242 were used to inhibit upstream regulators of PKBs (Supplementary Fig. 6a–f). In addition, recruitment of PKBA in wild-type cells with the dimerization system suppressed Ras-mediated PI(3)K activities (Fig. 3f and Supplementary Fig. 6g,h). Thus, the negative regulation by PKBs extends beyond RasC to other Ras small GTPases and PI(3)K. Interestingly, during chemotactic stimulation, activation of PKBs is delayed relative to the increase in Ras and PI(3)K activities[36,37,43], suggesting that they could act as a delayed negative feedback regulator of the excitable network.

Migratory profiles are dictated by properties of propagating STEN waves

To examine the changes in wave behaviour that accompanied the transitions to different migratory modes we monitored STEN and
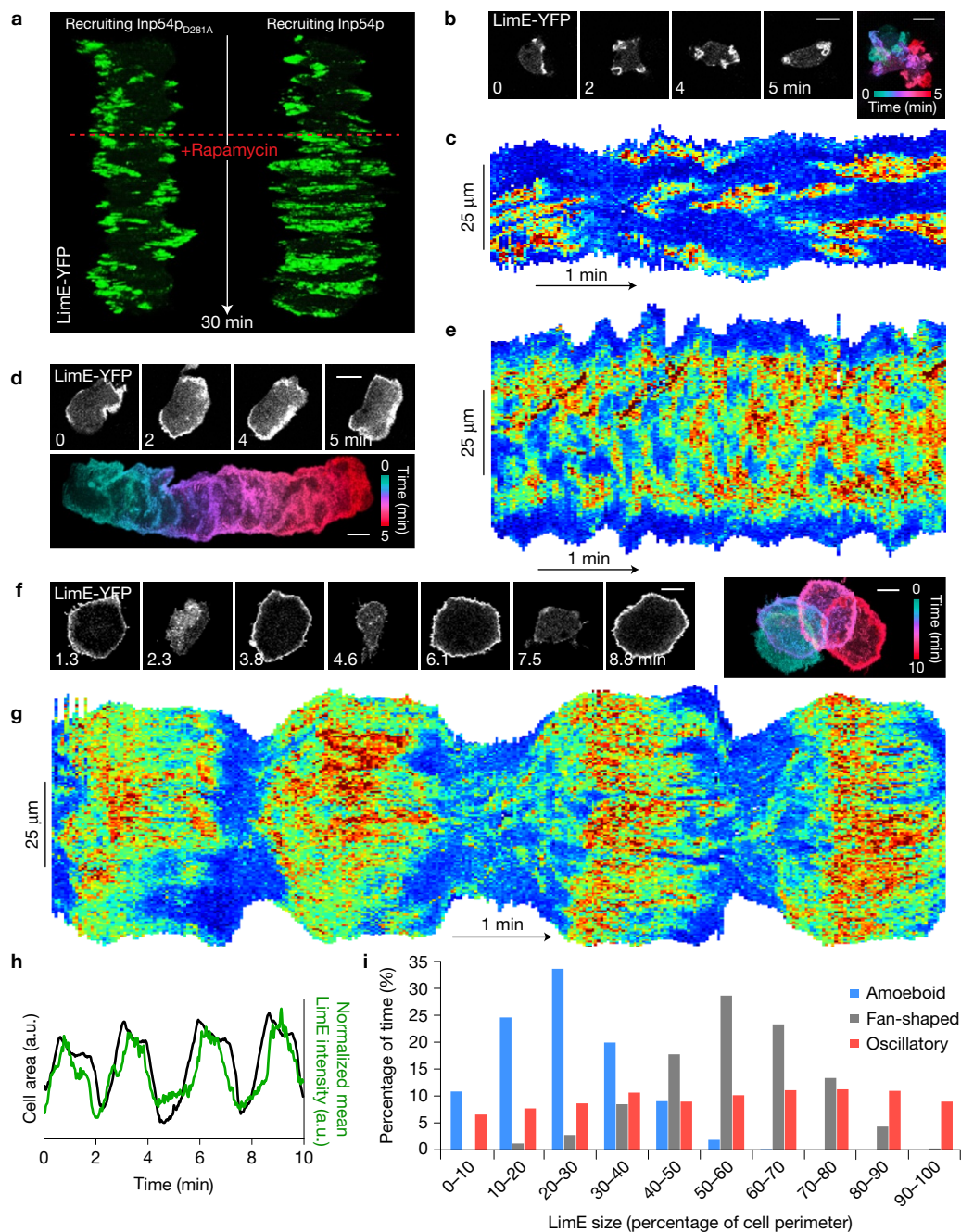
Figure 2 Actin profiles show distinct spatiotemporal patterns in amoeboid, fan-shaped and oscillatory cells. (**a**) T-stacks of LimE$_{\Delta coil}$-YFP (LimE) in initially amoeboid cells before and after recruiting inactive (left) or active (right) Inp54p. The red dashed line indicates the addition of rapamycin. (**b–g**) Time-lapse confocal images and colour-coded overlays of the YFP fluorescence intensities at 2 s intervals of an amoeboid (**b**), fan-shaped (**d**) and oscillatory cell (**f**) expressing LimE. Scale bars represent 10 μm. Kymographs of cortical LimE intensity in the same amoeboid (**c**), fan-shaped (**e**) and oscillatory cells (**g**). Durations of the kymographs are 5 min (**c**,**e**) and 10 min (**g**). (**h**) Temporal profiles of cell area (black) and normalized mean cortical LimE intensity (green) of the oscillatory cell above. Normalization for changes in cell shape is based on the kymograph of stably recruited mCherry-FRB-Inp54p intensity in the same cell as shown in Supplementary Fig. 5d. (**i**) Relative frequency of different LimE sizes (percentage of cell perimeter) appearing in each mode of migration (>2,000 time points combined from 10 kymographs of each mode automatically thresholded and quantified in MATLAB).

cytoskeletal activities, using biosensors PH$_{crac}$ and LimE, respectively, on the basal surface of cells by total internal reflection fluorescence (TIRF) microscopy (Fig. 4a,b and Supplementary Videos 8 and 9). As previously described in amoeboid cells, LimE and PH$_{crac}$ wave activities started at a point and propagated a few micrometres before

extinguishing. In oscillators, these activities began in a larger region, expanded in a wave that momentarily covered the basal surface of the cell, and then extinguished from the centre outward just before the cell collapsed. In fans, the expansion was similar except that it was not symmetric and did not extend to the rear of the cell and
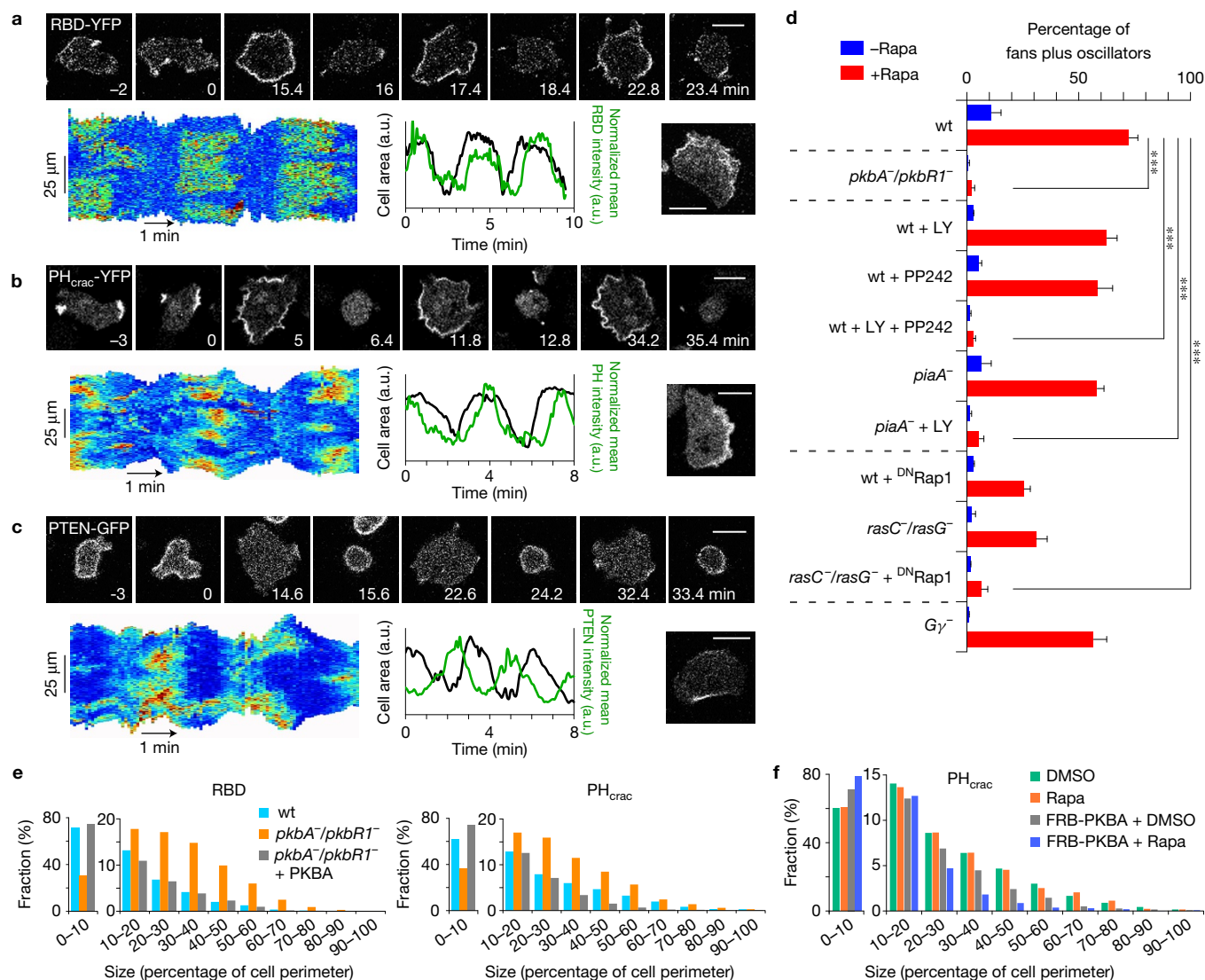
Figure 3 A signal transduction network mediates the transitions of cell migratory modes. (**a**–**c**) Dynamics of signal transduction biosensors RBD-YFP (**a**), PH$_{crac}$-YFP (**b**) and PTEN-GFP (**c**). In each panel: top, time-lapse confocal images of cells transitioning from amoeboid to oscillatory mode after rapamycin addition at time 0; bottom left, kymograph of cortical intensity of each biosensor in an oscillatory cell; bottom middle, temporal profile of cell area (black) and normalized mean cortical signalling intensity (green) in the corresponding oscillatory cell (normalization for changes in cell shape based on the kymograph of stably recruited mCherry-FRB-Inp54p intensity in the same cell as shown in Supplementary Fig. 5e–g.); bottom right, confocal image of a fan-shaped cell. Scale bars in all images represent 10 μm. (**d**) Percentage (mean ± s.d., $n=3$ experiments, >500 cells in each experiment, *** $P < 0.0001$, one-way ANOVA with *post hoc* Tukey HSD test) of fan-shaped plus oscillatory cells 10 min before (blue bars) and 10–20 min (red bars) after the addition of rapamycin at time 0. LY, LY294002. (**e**) Distributions of different sizes of RBD-GFP (left) and PH$_{crac}$-YFP (right) activity in cells of wild type (wt), *pkbA⁻/pkbR1⁻*-and *pkbA⁻/pkbR1⁻*-overexpressing PKBA. Cells were treated with 5 μM latrunculin A for 30 min. (**f**) Distributions of different sizes of PH$_{crac}$-YFP activity in wt cells, as well as wt cells expressing myr-FKBP-FKBP plus PKBA-mCherry-FRB, treated with DMSO or rapamycin in addition to 5 μM latrunculin A for 30 min. More than 3,000 cells from 3 independent experiments were analysed in each condition in **e**,**f**.

therefore pushed out a wide band on the front. This was often followed immediately by another asymmetric wave that kept the cell gliding in the same direction. Note that LimE and PH$_{crac}$ maintain the same relative distribution pattern (Fig. 4c and Supplementary Video 10) as previously published[44]. Consistent with the increased width and range, the waves in fans and oscillators move faster (Fig. 4d).

Next we assessed whether the increased STEN wave activities require an intact cytoskeleton. In cells immobilized with latrunculin A, PH$_{crac}$ still exhibited occasional flashes at the cell membrane. After Inp54p recruitment these patches became more frequent and larger

(Fig. 4e and Supplementary Video 11). Kymographs of individual cells show that PH$_{crac}$ as well as PTEN began to exhibit periodic waves along the periphery (Fig. 4f,g). Thus, the switch in the dynamic behaviour of the STEN is independent of the actin cytoskeleton or the normally accompanying morphological changes.

The altered wave properties can be traced to changes in the threshold for STEN activation

The expanded STEN waves could indicate that the threshold to activate the excitable network is lowered. To assess the sensitivity of
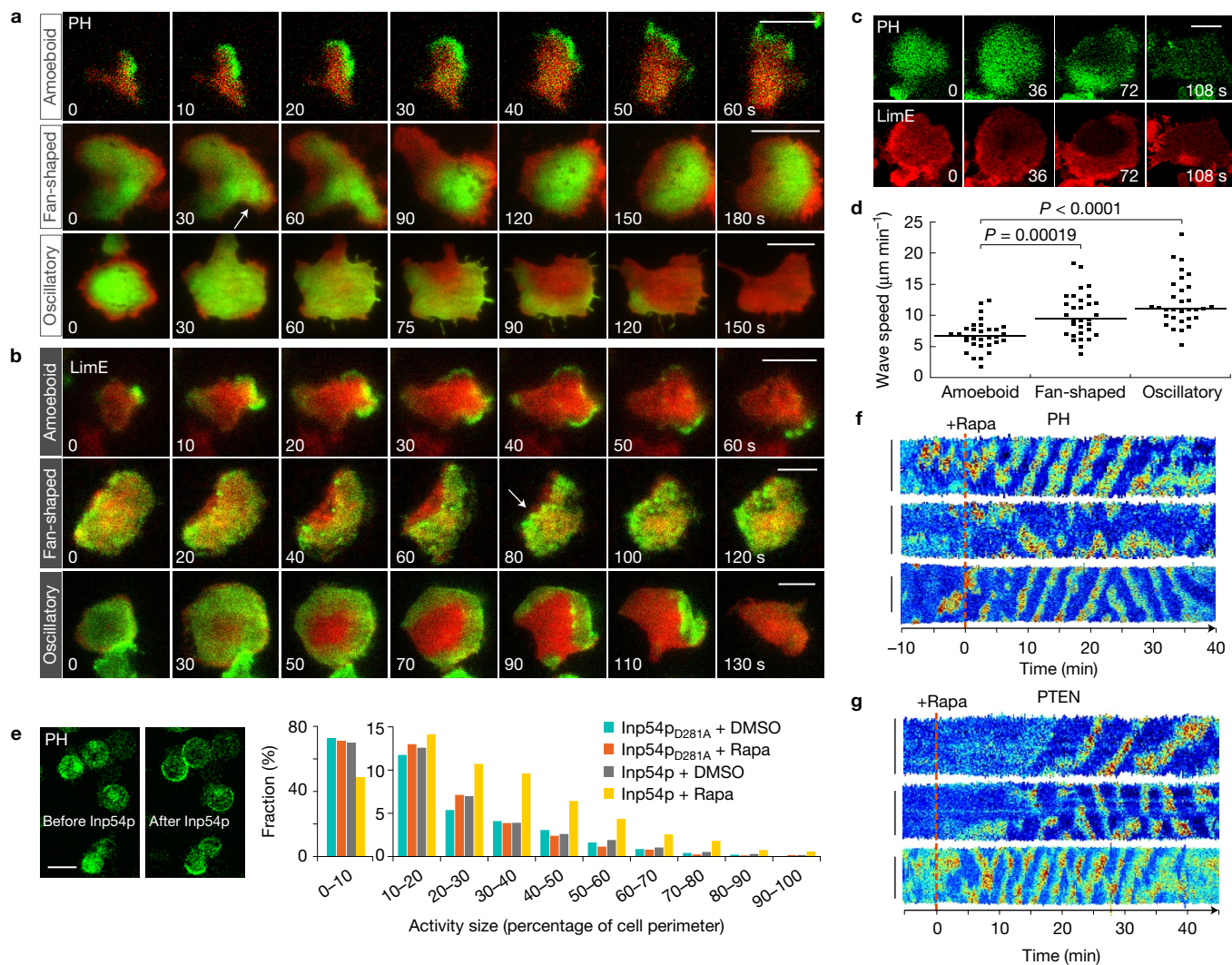
Figure 4 Properties of the STEN waves are altered independent of cytoskeleton. (**a,b**) Merged time-lapse TIRF micrographs of each mode of migration. PH$_{crac}$-YFP (green) and mCherry-FRB-Inp54p (red) are shown in **a**, and LimE-YFP (green) and mCherry-FRB-Inp54p (red) in **b**. The mCherry-FRB-Inp54p signals serve as membrane markers following recruitment. The white arrows point to new waves initiating at the front of fan-shaped cells. (**c**) Time-lapse TIRF micrographs of PH$_{crac}$-YFP (green) and LimE-RFP (red) in the same oscillatory cell. (**d**) Scatter plot of wave speed in each mode of migration ($n=31$ cells for each mode and the horizontal lines indicate median, $P=0.00019$ comparing amoeboid and fan-shaped, $P<0.0001$ comparing amoeboid and oscillator, Wilcoxon–Mann–Whitney rank sum test). (**e**) PH$_{crac}$-YFP activities in latrunculin-A-treated cells. Left, confocal images of PH$_{crac}$-YFP in the same cells before and after Inp54p recruitment. Right, distributions of different sizes of PH$_{crac}$-YFP activity in cells expressing mCherry-FRB-Inp54p$_{D281A}$ or mCherry-FRB-Inp54p (in addition to myr-FKBP-FKBP) treated with DMSO or rapamycin for 30 min. More than 3,000 cells from 3 independent experiments were analysed in each condition. (**f,g**) Kymographs of cortical PH$_{crac}$-YFP (**f**) or PTEN-GFP (**g**) intensity in cells treated with 5 μM latrunculin A. The red dashed lines indicate time 0 at which rapamycin was added. Solid vertical lines on the left of each kymograph represent 20 μm. Scale bars in all images represent 10 μm.

the STEN, we monitored the translocation of PH$_{crac}$ in response to chemoattractant in the same cells before and after Inp54p recruitment. Figure 5a shows that the same set of cells, which did not respond to low amounts of cyclic AMP, did respond to the same dose after Inp54p recruitment, while the responses to saturating levels of stimulus were nearly identical (Fig. 5b). Further, the concentration of cAMP eliciting a half-maximal response shifted from about 1 nM to 200 pM after lowering PtdIns(4,5)P$_2$ levels (Fig. 5c), which was not observed when recruiting inactive Inp54p$_{D281A}$ (Fig. 5d). Recruiting RasC$_{Q62L(\Delta CAAX)}$ also slightly left-shifted the dose–response curve to cAMP (Supplementary Fig. 7). These results suggest that the

perturbations that bring about expanded waves and migratory mode transitions also increase the excitability of the STEN.

Simulations altering the threshold of excitable network capture the entire spectrum of cell behaviours

To see the effect of perturbations on an excitable system, we simulated an activator–inhibitor system coupled to a polarization module using stochastic, partial-differential equations on a 2D surface (Methods and Supplementary Fig. 8a,b). The model was parameterized to recreate the pattern of activity seen in amoeboid cells. Simulations recreated waves of activity seen by TIRF that propagate outward and extinguish
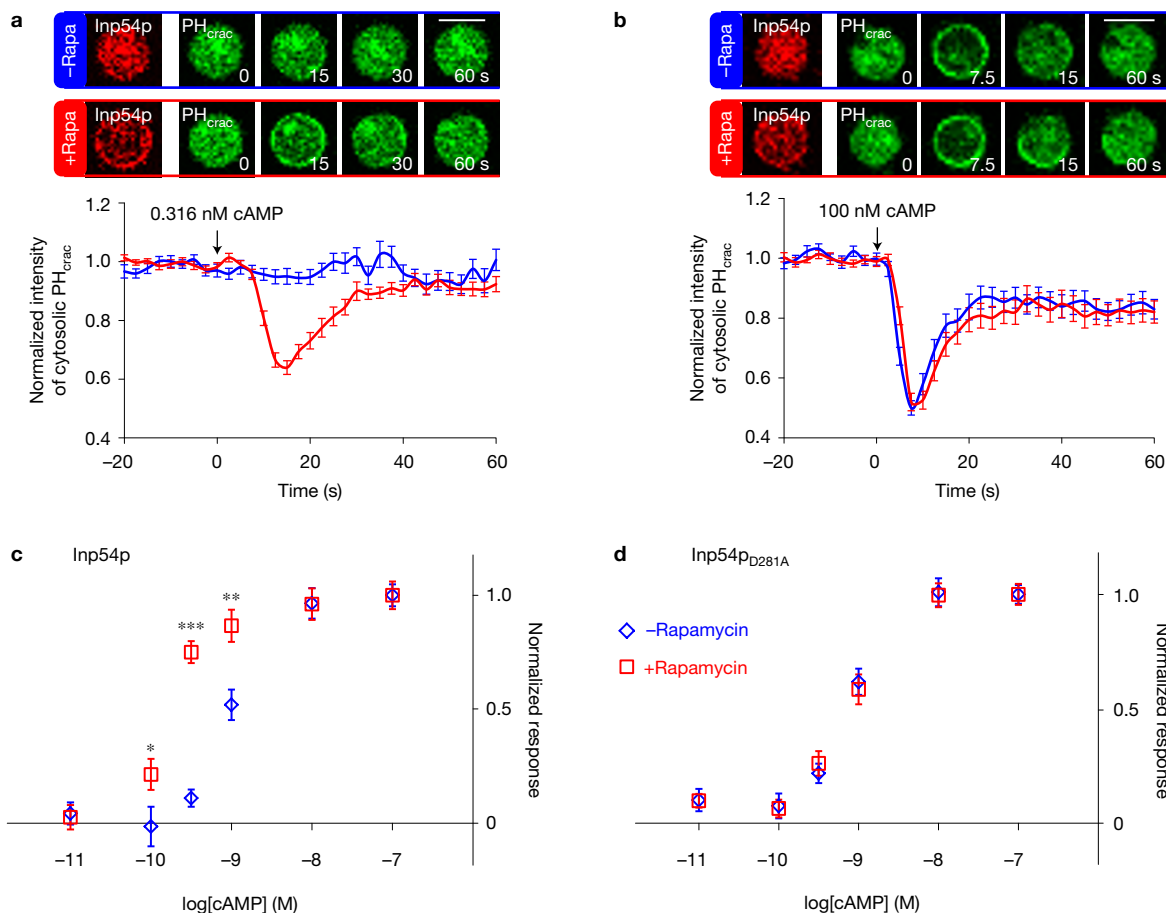
Figure 5 The threshold for STEN activation is lowered. (**a**,**b**) Responses of PH$_{crac}$-YFP to global cAMP stimulations in the same cells before (blue box) and after (red box) Inp54p recruitment. Top, time-lapse confocal images of PH$_{crac}$ (green) and mCherry-FRB-Inp54p (red). cAMP was added at time 0 (316 pM cAMP in **a** and 100 nM cAMP in **b**). Scale bars represent 10 μm. Bottom, temporal profiles of normalized mean cytosolic PH$_{crac}$ intensity, with the blue line indicating before and red indicating after rapamycin treatment (mean ± s.e.m., $n = 26$ cells for **a** and $n = 18$ cells for **b**). (**c**,**d**) Normalized PH$_{crac}$ responses (drop of cytosolic intensity) to different doses of cAMP before (blue) and after (red) rapamycin. (**c**) Recruiting Inp54p. (**d**) Recruiting inactive Inp54p. Response in each individual condition was normalized to that following 100 nM cAMP stimulation (mean ± s.e.m., from the lowest to the highest cAMP concentrations, $n = 24$, 21, 26, 21, 25, 18 cells in **c**, and $n = 21$, 21, 23, 23, 21, 23 cells in **d**, $^{*}P = 0.046$, $^{**}P = 0.002$, $^{***}P < 0.0001$, two-tailed t-test).

relatively quickly (Fig. 6a and Supplementary Video 12). When we lowered only the threshold for triggering excitable behaviour, we observed more robust waves that travelled faster and farther. The frequency of firings also increased leading to more waves being present at any time (Fig. 6b). After additional reduction of the threshold, nearly the whole field underwent synchronized periods of activity and inactivity (Fig. 6c).

We used a 1D model of the excitable system coupled to a viscoelastic cell model in the level set framework to determine the effect of these changes on cell migratory modes[27]. In these simulations, initially randomly extended projections gradually became localized toward the front as the cells polarized (Fig. 6d and Supplementary Video 13). As we lowered the threshold, the waves that guided projections moved faster and spread further to cover roughly half of the cell and were triggered periodically while the back remained quiescent (Fig. 6e and Supplementary Video 13), resulting in a fan-shaped cell. When the threshold was further reduced, multiple initiations appeared and the waves rapidly encompassed the whole cell causing it to spread. This symmetric response was closely followed by a retraction as

the waves extinguished, before starting the next cycle (Fig. 6f and Supplementary Video 13).

The migratory mode transitions were observed in a single simulation by gradually lowering the threshold (Fig. 6g). Plotting the mean and maximum intensity of either the activator or the inhibitor of the excitable network over the perimeter as a function of time revealed behaviour that coincided with different modes: the mean activity of amoeboid cells is low, but the maximum is high and fluctuates; in fans, the maximum is persistently high, but the mean increases as the size of the active zone expands; and in oscillators, the maximum and mean levels of activity always coincide (Fig. 6g and Supplementary Fig. 8c). During the transition from amoeboid to fan-shaped, the front of the cell expanded outward while the back of the cell retracted (Supplementary Video 14). As the cell transitioned from fan-shaped to oscillatory, the activity spread instantly around the entire perimeter as the cell spread and then disappeared causing the contraction (Supplementary Video 14).

To recreate cell-to-cell heterogeneity, we continuously lowered the threshold as above but randomized its initial and final values
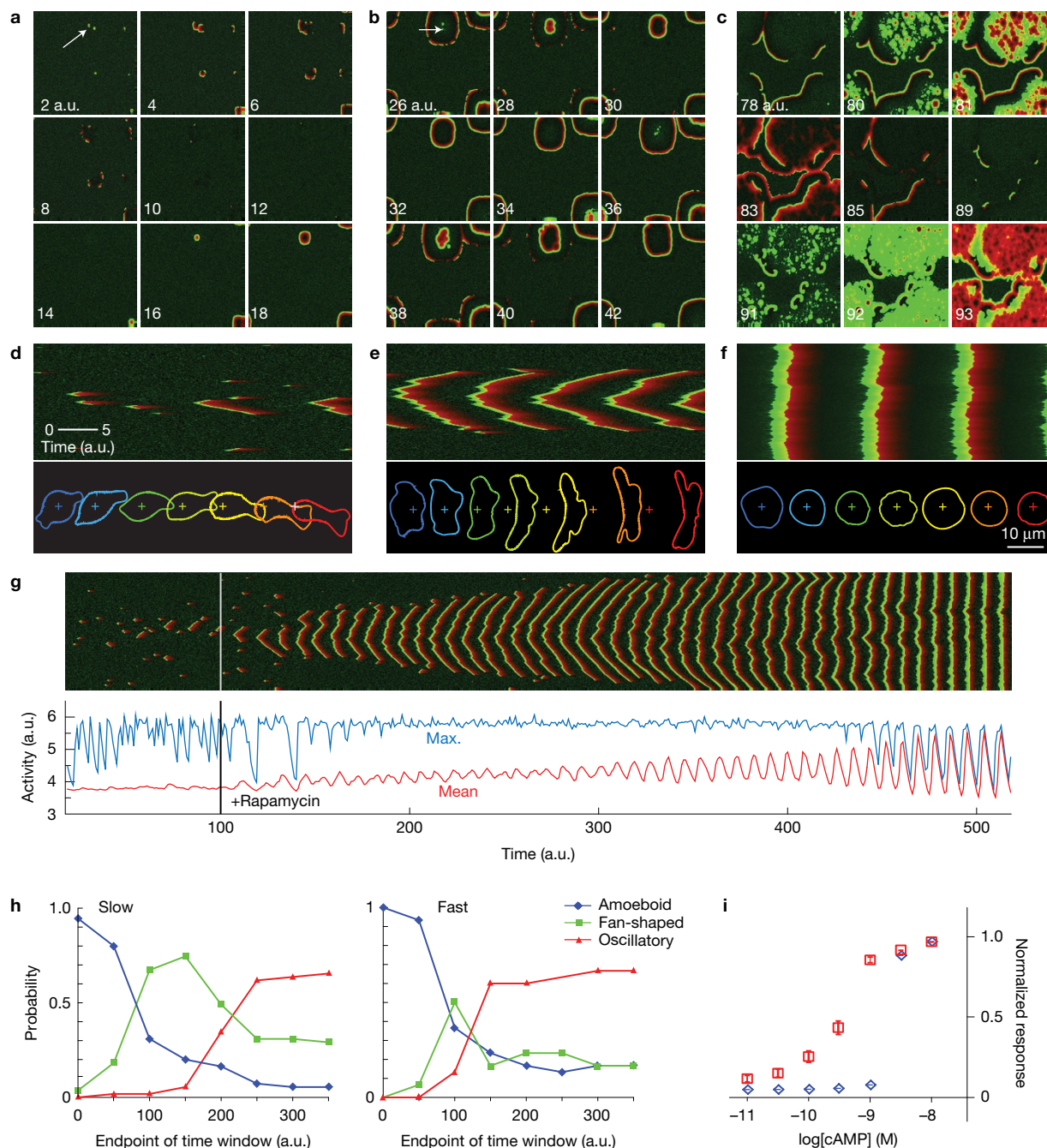
Figure 6 Simulations of the excitable network with varying thresholds successfully capture various cell migratory modes. (**a–c**) Two-dimensional simulations showing waves of activity propagating outward and extinguishing, with gradually decreasing threshold from **a** to **c**. Green and red represent the activator (F) and inhibitor (R) activities, respectively. Yellow denotes the region where the two overlap. Arrows point to the initiation of new waves. (**d–f**) Kymographs (top) and simulated cell morphologies (bottom) give rise to amoeboid, fan-shaped and oscillatory behaviours, respectively. The cell shapes are colour-coded from blue to red, showing the same cell at in different times; the coloured crosses denote a fixed origin. (**g**) Kymograph (top) of the response to a gradual threshold decrease over a larger timescale. The threshold was held constant until $t = 100$ (solid line), after which it was lowered exponentially. The lower plots show the maximum (blue) and mean (red) levels of activity. (**h**) Fraction of cells in one of the three migratory modes as a function of time, with slowly (left) and rapidly (right) decreasing threshold obtained from simulations of 45–55 cells. (**i**) Normalized response curve to different levels of external stimuli (cAMP) for higher (blue) and lower (red) thresholds. Normalization is with respect to the 100 nM cAMP response.

in different cells. At each time point, different migratory modes were observed among the cell population. As was observed experimentally, the predominant mode shifted in time from amoeboid to fan-shaped to oscillatory (Fig. 6h). Curiously, we occasionally saw

'reverse' shifts such as ones from oscillatory to fan-shaped cells in the simulation, similar to those observed in cells (compare Fig. 1e and Supplementary Fig. 8c). We also altered the rate at which we lowered the threshold and observed that the transition away from
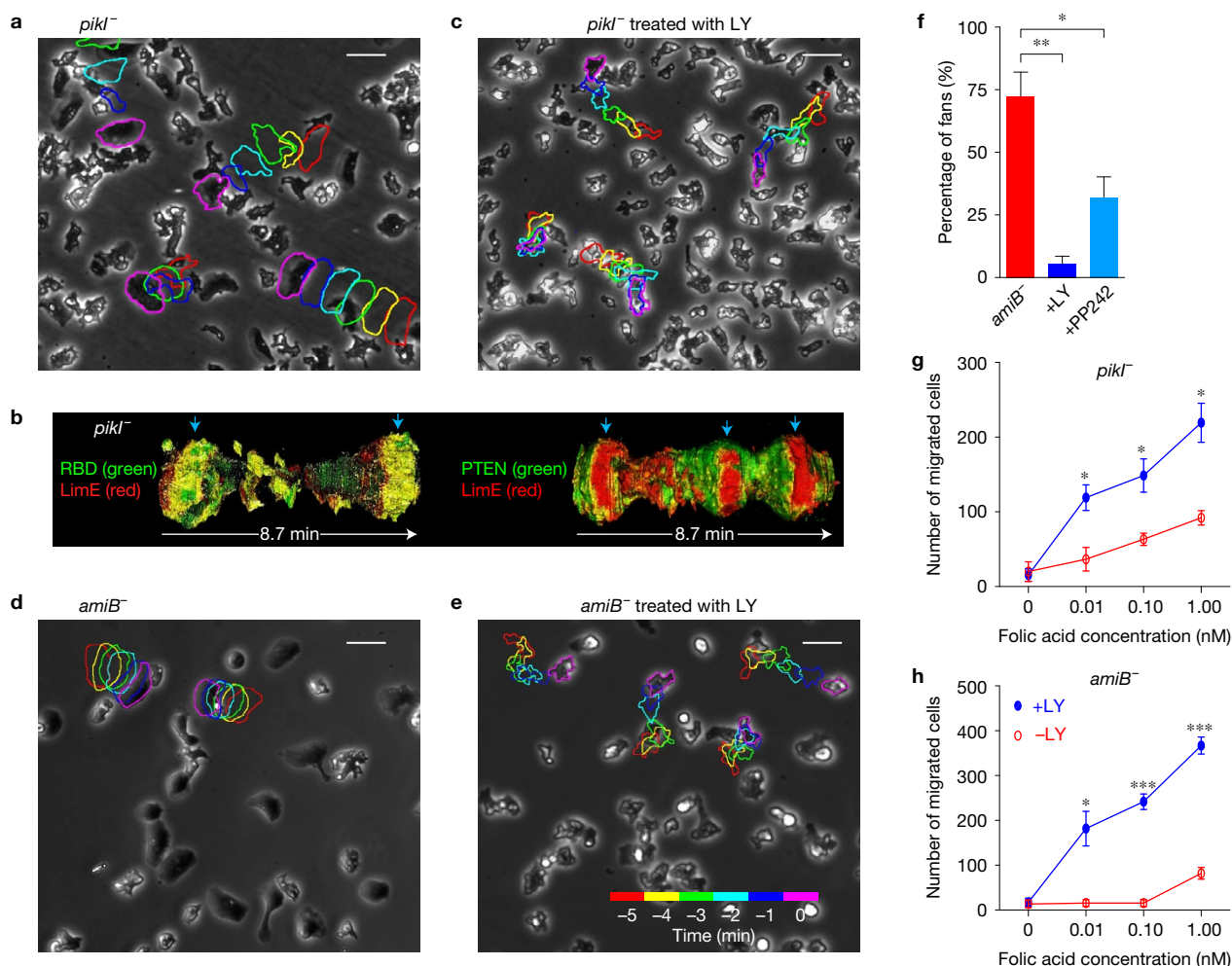
Figure 7 Innately fan-shaped or oscillatory cells can be converted to amoeboid mode. (**a**–**e**) Phase-contrast images of *pikI⁻* (**a**,**c**) and *amiB⁻* cells (**d**,**e**) treated with (**c**,**e**) or without (**a**,**d**) LY294002 (LY). Colour-coded outlines (1 min apart) of several cells were imposed on top of the phase images, with magenta outlining the current cells. Scale bars represent 25 μm. *T*-stacks (**b**) of merged confocal images of oscillatory *pikI⁻* cells expressing RBD-YFP and LimE-RFP (left) or PTEN-GFP and LimE-RFP (right). Blue arrows indicate the spreading phases during the oscillation. (**f**) Percentage of fan-shaped cells in *amiB⁻* before and after 30 μM LY treatment, and after 20 μM PP242 treatment (mean ± s.d., $n=3$ experiments, >100 cells in each experiment, *$P=0.0043$, **$P=0.0002$, one-way ANOVA with *post hoc* Tukey HSD test). (**g**,**h**) Chemotaxis assays before (red) and after (blue) LY treatment of *pikI⁻* (**g**) and *amiB⁻* (**h**) cells. Numbers of cells migrating through pores into folic-acid-filled chambers and controls are shown (mean ± s.e.m., $n=3$ experiments, >7,500 cells in each experiment, *$P=0.0036$, 0.0033, 0.0013 in **g**, *$P=0.0019$ and ***$P<0.0001$ in **h**, two-tailed *t*-test).

amoeboid cells was faster for higher rates of reduction (Fig. 6h) as seen experimentally (Fig. 1f). Finally, we simulated the dose–response behaviour of a heterogeneous population of cells before and after lowering the threshold. The curves showed a left shift (Fig. 6i) matching the experimental observations (Fig. 5c).

Conversion of innately fan-shaped or oscillatory cells to amoeboid mode recovers directed migration

We examined *pikI⁻* cells lacking a major PIP-5-kinase[45] (PI(5)K), which were reported to have decreased PtdIns(4,5)P₂ levels and to fail to perform chemotaxis. We observed many fan-shaped or oscillatory cells in the population (Fig. 7a and Supplementary Video 15). Further, cytoskeletal and signal transduction biosensors exhibited identical patterns in these oscillatory cells as in those induced by acute perturbations (Fig. 7b). As this suggested the presence of excess STEN activity, we reasoned that inhibition of the coupling of these events to

the cytoskeleton could convert the cells to the amoeboid mode. Indeed, addition of PI(3)K inhibitor caused the cells to round up initially. Remarkably, within about 30 min more than 90% cells were moving in the amoeboid mode (Fig. 7c and Supplementary Video 15).

A previously reported mutant, *amiB⁻* (ref. 46), consists of almost entirely fan-shaped cells when starved (Fig. 7d). The migration profile of these cells is similar to those we produced with our acute perturbations. As above we treated *amiB⁻* fan-shaped cells with the PI(3)K inhibitor. The *amiB⁻* cells initially rounded up, but within 30 min, greater than 70% of *amiB⁻* cells recovered and continued to move in the amoeboid mode for a couple of hours (Fig. 7e,f and Supplementary Video 16). The TORC2 inhibitor PP242 had a similar effect (Fig. 7f).

Consistent with previous results we observed that both *pikI⁻* and *amiB⁻* cells failed to carry out chemotaxis over the range of folic acid gradients. We speculated that the excess STEN activities in these cells might impair directed migration and that conversion of the cells
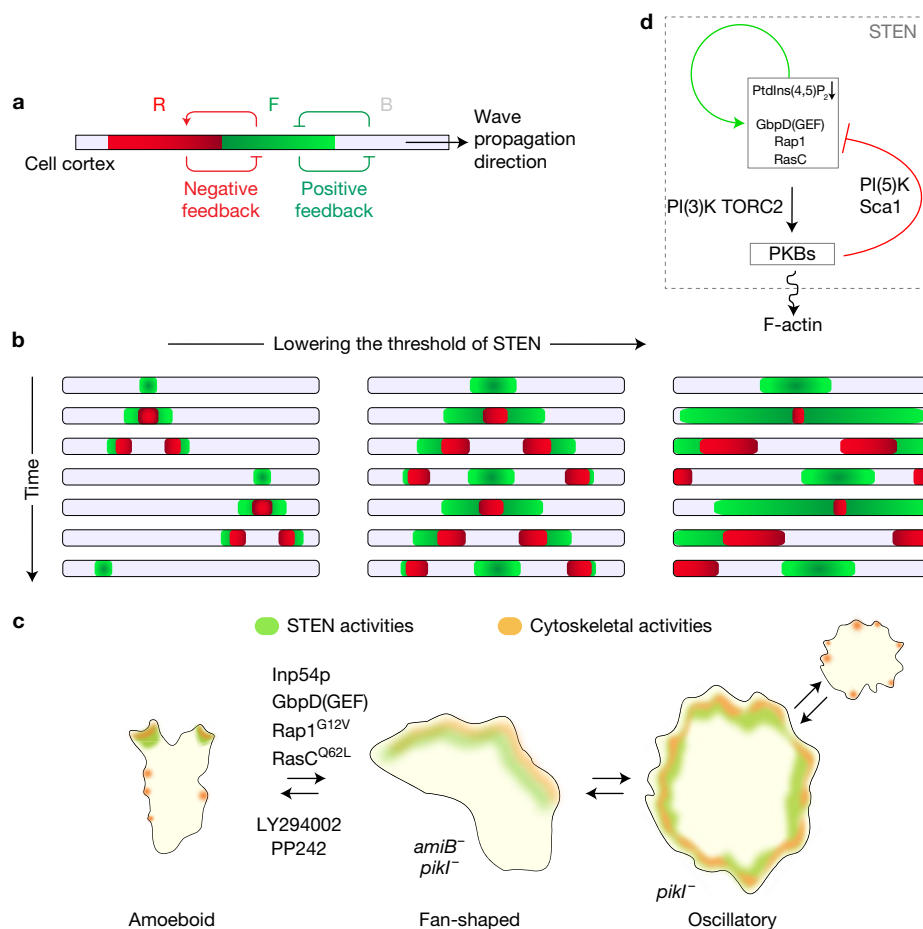
Figure 8 Propagating waves of STEN activity control cell migratory modes. (**a**) Snapshot of the cortical membrane showing regions where the STEN is in B- (grey), F- (green) and R- (red) states. Positive feedback, depicted as mutual inhibition between F- and B-states, and negative feedback from R- to F-states, together with diffusion of network components, advances the wave unidirectionally (black arrow). (**b**) During amoeboid migration (left), network activities initiate locally and spread in waves that dissipate over a short distance. Since the F-state organizes cytoskeletal activities, this pattern controls the formation of pseudopodia. When the threshold of the network is lowered (middle), the waves initiate at larger zones and spread faster and further around the cell before dissipating. When the threshold is further lowered (right), initiated waves propagate even further to swiftly cover the nearly entire membrane. The colour scheme is same as in **a**. (**c**) Schematic representation of STEN and cytoskeletal activities in amoeboid, fan-shaped and oscillatory cells. (**d**) Proposed molecular architecture of STEN. PtdIns(4,5)P$_2$ levels antagonize while GbpD(GEF), Rap1 and RasC promote the positive feedback loop (green) of the excitable network. PKBs serve in a delayed negative feedback loop (red) through a set of their substrates including Sca1 and PI(5)K, and promote F-actin through other sets of substrates.

to amoeboid modes of migration might restore their ability to move up chemotactic gradients. Indeed, after treatment with the PI(3)K inhibitor, both *pikI*⁻ and *amiB*⁻ cells displayed greatly improved chemotaxis to every folic acid concentration tested (Fig. 7g,h).

DISCUSSION

Our results show that various cell migratory modes arise from different thresholds of an excitable signal transduction network. In simulations, small decreases in the threshold of an excitable network were sufficient to expand the range of waves to cover increasing fractions of the cell perimeter, and this led to dramatic changes in protrusions and cell migratory modes. Our experimental results demonstrate a causal chain of events where changing the threshold alters the range of propagating STEN waves and in turn cytoskeletal activities and the nature of cellular protrusions, which promotes transitions among migratory modes.

We propose that local regions of the cell cortex transition between inactive and active states, which we designate as B and F, respectively, since 'back' and 'front' markers such as PTEN and PI(3)K tend to associate with these regions (Fig. 8a). We propose that a refractory state, R, follows the F-state. The B- and F-states are mutually inhibitory, creating a positive feedback loop. The F- and R-states are related through a delayed negative feedback loop. In resting cells, most of the cortex is in the B-state. Once initiated, waves propagate unidirectionally because diffusion of F-state components triggers activation in adjoining B- but not R-regions. Lowering the threshold for activation promotes the F-state, thereby increasing the speed and range of the propagating waves, leading to fans and oscillators (Fig. 8b,c). Bear in mind that the schematic diagram in Fig. 8b is a 1D representation of the more-or-less circular waves propagating on the cell cortex as seen in the TIRF videos and in the 2D simulations. The coupling of the F-state waves to cytoskeleton we have proposed

explains the expanding cup-like structures observed by lattice light sheet microscopy of randomly migrating *Dictyostelium* cells[47,48].

Our results provide important guidelines for the molecular architecture that confers excitability to the network (Fig. 8d). Our studies implicate RasC, Rap1, GbpD, PtdIns(4,5)P$_2$ and PKBR1/PKBA in the feedback loops that regulate the transitions between states of the cell cortex. They suggest that activation of Ras/Rap-related activities, or lowering PtdIns(4,5)P$_2$, promotes positive feedback. The PKBs appear to have dual roles. On one hand, they are strong candidates for the delayed negative feedback that resolves the activation since STEN activities were elevated in cells lacking both PKBs and were suppressed following recruitment of PKBA (Fig. 3e,f and Supplementary Fig. 6). These are consistent with previous reports suggesting that PKBs indirectly inhibit Ras GEF Aimless[36] and directly activate PI(5)K[43], which would increase PtdIns(4,5)P$_2$ levels. On the other hand, probably through a different set of substrates, the PKBs are required to link the elevated STEN activities to the cytoskeleton since their inhibition blocked expanded protrusions (Fig. 3d).

We found that decreasing PtdIns(4,5)P$_2$ levels effectively lowered the threshold of the STEN even in the absence of F-actin (Fig. 4e–g). PtdIns(4,5)P$_2$ has been reported to play diverse roles in cytoskeletal organization and regulation[49–54]. We speculate that lowering PIP2 levels might function by promoting the activation of multiple Ras and Rap proteins. Activated Ras signals were detected at the entire periphery of induced spreading cells (Fig. 3a), and acutely increasing Ras or Rap activities had a similar effect to lowering PtdIns(4,5)P$_2$ levels (Supplementary Video 5). Furthermore, combined inhibition of several Ras and Rap GTPases blocked the migratory mode transitions induced by decreasing PtdIns(4,5)P$_2$ (Fig. 3d).

We propose that directional sensing could be achieved if an extracellular cue lowered the threshold at the front and raised it at the back. Thus, there would be more and larger protrusions at the front compared with the back, which could bring about guidance with high sensitivity. Of course, directed cell migration would be impaired at either end of the dynamic range. In fact, manipulations of *amiB*$^-$ and *pikI*$^-$ cells showed that amoeboid outperformed oscillatory and keratocyte-like fan-shaped cells in chemotaxis (Fig. 7g,h). Inhibition of PI(3)K is effective in restoring the chemotactic ability of *pikI*$^-$ cells, implying that the system can still function with lowered PtdIns(4,5)P$_2$ and PtdIns(3,4,5)P$_3$ levels. Thus, what is important for proper chemotaxis is an optimal level of STEN activity and cytoskeletal coupling, rather than simply the activity or amount of a certain molecule.

The STEN wave scheme of cell migration has important implications. First, it can explain why diverse cell types display predominantly different migratory modes, since the resting set point of a cell is expected to be determined intrinsically by the expression profiles of network components. Second, it would allow cells to rapidly adjust behaviour to various environments, using nearly the same components, which might underlie the plasticity of migrating cells such as during cancer metastasis. Third, it enables a cell to integrate multiple chemical and mechanical cues, if they all fed into controlling the threshold of the same STEN. Finally, the natural heterogeneity in the set points of the STEN among individual cells within a population can lead to different behaviours and a range of responses to the same cue, facilitating sorting and patterning. ☐

METHODS

Methods, including statements of data availability and any associated accession codes and references, are available in the online version of this paper.

Note: Supplementary Information is available in the online version of the paper

1. Bosgraaf, L. & Van Haastert, P. J. The ordered extension of pseudopodia by amoeboid cells in the absence of external cues. *PLoS ONE* **4**, e5253 (2009).
2. Barnhart, E. L., Allen, G. M., Julicher, F. & Theriot, J. A. Bipedal locomotion in crawling cells. *Biophys. J.* **98**, 933–942 (2010).
3. Mattila, P. K. & Lappalainen, P. Filopodia: molecular architecture and cellular functions. *Nat. Rev. Mol. Cell Biol.* **9**, 446–454 (2008).
4. Krause, M. & Gautreau, A. Steering cell migration: lamellipodium dynamics and the regulation of directional persistence. *Nat. Rev. Mol. Cell Biol.* **15**, 577–590 (2014).
5. Reichman-Fried, M., Minina, S. & Raz, E. Autonomous modes of behavior in primordial germ cell migration. *Dev. Cell* **6**, 589–596 (2004).
6. Chan, C. *et al.* A model for migratory B cell oscillations from receptor down-regulation induced by external chemokine fields. *Bull. Math. Biol.* **75**, 185–205 (2013).
7. Friedl, P. & Alexander, S. Cancer invasion and the microenvironment: plasticity and reciprocity. *Cell* **147**, 992–1009 (2011).
8. Yilmaz, M. & Christofori, G. Mechanisms of motility in metastasizing cells. *Mol. Cancer Res.* **8**, 629–642 (2010).
9. Artemenko, Y., Axiotakis, L. Jr, Borleis, J., Iglesias, P. A. & Devreotes, P. N. Chemical and mechanical stimuli act on common signal transduction and cytoskeletal networks. *Proc. Natl Acad. Sci. USA* **113**, E7500–E7509 (2016).
10. Sasaki, A. T. *et al.* G protein-independent Ras/PI3K/F-actin circuit regulates basic cell motility. *J. Cell Biol.* **178**, 185–191 (2007).
11. Huang, C. H., Tang, M., Shi, C., Iglesias, P. A. & Devreotes, P. N. An excitable signal integrator couples to an idling cytoskeletal oscillator to drive cell migration. *Nat. Cell Biol.* **15**, 1307–1316 (2013).
12. Swaney, K. F., Huang, C. H. & Devreotes, P. N. Eukaryotic chemotaxis: a network of signaling pathways controls motility, directional sensing, and polarity. *Annu. Rev. Biophys.* **39**, 265–289 (2010).
13. Artemenko, Y., Lampert, T. J. & Devreotes, P. N. Moving towards a paradigm: common mechanisms of chemotactic signaling in Dictyostelium and mammalian leukocytes. *Cell. Mol. Life Sci.* **71**, 3711–3747 (2014).
14. Bear, J. E. & Haugh, J. M. Directed migration of mesenchymal cells: where signaling and the cytoskeleton meet. *Curr. Opin. Cell Biol.* **30**, 74–82 (2014).
15. Pocha, S. M. & Montell, D. J. Cellular and molecular mechanisms of single and collective cell migrations in Drosophila: themes and variations. *Annu. Rev. Genet.* **48**, 295–318 (2014).
16. Xiong, Y., Huang, C. H., Iglesias, P. A. & Devreotes, P. N. Cells navigate with a local-excitation, global-inhibition-biased excitable network. *Proc. Natl Acad. Sci. USA* **107**, 17079–17086 (2010).
17. Nishikawa, M., Horning, M., Ueda, M. & Shibata, T. Excitable signal transduction induces both spontaneous and directional cell asymmetries in the phosphatidyl-inositol lipid signaling system for eukaryotic chemotaxis. *Biophys. J.* **106**, 723–734 (2014).

18. Gerisch, G., Ecke, M., Wischnewski, D. & Schroth-Diez, B. Different modes of state transitions determine pattern in the Phosphatidylinositide-Actin system. *BMC Cell Biol.* **12,** 42 (2011).

19. Gerisch, G., Schroth-Diez, B., Muller-Taubenberger, A. & Ecke, M. PIP3 waves and PTEN dynamics in the emergence of cell polarity. *Biophys. J.* **103,** 1170–1178 (2012).

20. Vicker, M. G. Eukaryotic cell locomotion depends on the propagation of self-organized reaction-diffusion waves and oscillations of actin filament assembly. *Exp. Cell Res.* **275,** 54–66 (2002).

21. Arai, Y. *et al.* Self-organization of the phosphatidylinositol lipids signaling system for random cell migration. *Proc. Natl Acad. Sci. USA* **107,** 12399–12404 (2010).

22. Taniguchi, D. *et al.* Phase geometries of two-dimensional excitable waves govern self-organized morphodynamics of amoeboid cells. *Proc. Natl Acad. Sci. USA* **110,** 5016–5021 (2013).

23. Asano, Y., Nagasaki, A. & Uyeda, T. Q. Correlated waves of actin filaments and PIP3 in *Dictyostelium* cells. *Cell Motil. Cytoskeleton* **65,** 923–934 (2008).

24. Giannone, G. *et al.* Periodic lamellipodial contractions correlate with rearward actin waves. *Cell* **116,** 431–443 (2004).

25. Weiner, O. D., Marganski, W. A., Wu, L. F., Altschuler, S. J. & Kirschner, M. W. An actin-based wave generator organizes cell motility. *PLoS Biol.* **5,** e221 (2007).

26. Case, L. B. & Waterman, C. M. Adhesive F-actin waves: a novel integrin-mediated adhesion complex coupled to ventral actin polymerization. *PLoS ONE* **6,** e26631 (2011).

27. Shi, C., Huang, C. H., Devreotes, P. N. & Iglesias, P. A. Interaction of motility, directional sensing, and polarity modules recreates the behaviors of chemotaxing cells. *PLoS Comput. Biol.* **9,** e1003122 (2013).

28. Shibata, T., Nishikawa, M., Matsuoka, S. & Ueda, M. Intracellular encoding of spatiotemporal guidance cues in a self-organizing signaling system for chemotaxis in *Dictyostelium* cells. *Biophys. J.* **105,** 2199–2209 (2013).

29. Hecht, I. *et al.* Activated membrane patches guide chemotactic cell motility. *PLoS Comput. Biol.* **7,** e1002044 (2011).

30. Neilson, M. P. *et al.* Chemotaxis: a feedback-based computational model robustly predicts multiple aspects of real cell behaviour. *PLoS Biol.* **9,** e1000618 (2011).

31. Nagel, O. *et al.* Geometry-driven polarity in motile amoeboid cells. *PLoS ONE* **9,** e113382 (2014).

32. Cooper, R. M., Wingreen, N. S. & Cox, E. C. An excitable cortex and memory model successfully predicts new pseudopod dynamics. *PLoS ONE* **7,** e33528 (2012).

33. Kortholt, A., King, J. S., Keizer-Gunnink, I., Harwood, A. J. & Van Haastert, P. J. Phospholipase C regulation of phosphatidylinositol 3,4,5-trisphosphate-mediated chemotaxis. *Mol. Biol. Cell* **18,** 4772–4779 (2007).

34. Huang, Y. E. *et al.* Receptor-mediated regulation of PI3Ks confines PI(3,4,5)P3 to the leading edge of chemotaxing cells. *Mol. Biol. Cell* **14,** 1913–1922 (2003).

35. Bolourani, P., Spiegelman, G. & Weeks, G. Ras proteins have multiple functions in vegetative cells of *Dictyostelium*. *Eukaryot. Cell* **9,** 1728–1733 (2010).

36. Charest, P. G. *et al.* A Ras signaling complex controls the RasC-TORC2 pathway and directed cell migration. *Dev. Cell* **18,** 737–749 (2010).

37. Cai, H. *et al.* Ras-mediated activation of the TORC2-PKB pathway is critical for chemotaxis. *J. Cell Biol.* **190,** 233–245 (2010).

38. Kortholt, A. *et al.* A Rap/phosphatidylinositol 3-kinase pathway controls pseudopod formation. *Mol. Biol. Cell* **21,** 936–945 (2010).

39. Suh, B. C., Inoue, T., Meyer, T. & Hille, B. Rapid chemically induced changes of PtdIns(4,5)P2 gate KCNQ ion channels. *Science* **314,** 1454–1457 (2006).

40. DeRose, R., Miyamoto, T. & Inoue, T. Manipulating signaling at will: chemically-inducible dimerization (CID) techniques resolve problems in cell biology. *Pflugers Arch.* **465,** 409–417 (2013).

41. Ghosh, R. *et al.* Sec14-nodulin proteins and the patterning of phosphoinositide landmarks for developmental control of membrane morphogenesis. *Mol. Biol. Cell* **26,** 1764–1781 (2015).

42. Kortholt, A. *et al.* Characterization of the GbpD-activated Rap1 pathway regulating adhesion and cell polarity in *Dictyostelium discoideum*. *J. Biol. Chem.* **281,** 23367–23376 (2006).

43. Kamimura, Y. *et al.* PIP3-independent activation of TorC2 and PKB at the cell's leading edge mediates chemotaxis. *Curr. Biol.* **18,** 1034–1043 (2008).

44. Gerhardt, M. *et al.* Actin and PIP3 waves in giant cells reveal the inherent length scale of an excited state. *J. Cell Sci.* **127,** 4507–4517 (2014).

45. Fets, L., Nichols, J. M. & Kay, R. R. A PIP5 kinase essential for efficient chemotactic signaling. *Curr. Biol.* **24,** 415–421 (2014).

46. Asano, Y. *et al.* Keratocyte-like locomotion in amiB-null *Dictyostelium* cells. *Cell Motil. Cytoskeleton* **59,** 17–27 (2004).

47. Chen, B. C. *et al.* Lattice light-sheet microscopy: imaging molecules to embryos at high spatiotemporal resolution. *Science* **346,** 1257998 (2014).

48. Veltman, D. M. *et al.* A plasma membrane template for macropinocytic cups. *elife* **5,** e20085 (2016).

49. Raucher, D. *et al.* Phosphatidylinositol 4,5-bisphosphate functions as a second messenger that regulates cytoskeleton-plasma membrane adhesion. *Cell* **100,** 221–228 (2000).

50. Ueno, T., Falkenburger, B. H., Pohlmeyer, C. & Inoue, T. Triggering actin comets versus membrane ruffles: distinctive effects of phosphoinositides on actin reorganization. *Sci. Signal.* **4,** ra87 (2011).

51. van Rheenen, J. *et al.* EGF-induced PIP2 hydrolysis releases and activates cofilin locally in carcinoma cells. *J. Cell Biol.* **179,** 1247–1259 (2007).

52. Hartwig, J. H. *et al.* Thrombin receptor ligation and activated Rac uncap actin filament barbed ends through phosphoinositide synthesis in permeabilized human platelets. *Cell* **82,** 643–653 (1995).

53. Glogauer, M., Hartwig, J. & Stossel, T. Two pathways through Cdc42 couple the N-formyl receptor to actin nucleation in permeabilized human neutrophils. *J. Cell Biol.* **150,** 785–796 (2000).

54. Prehoda, K. E., Scott, J. A., Mullins, R. D. & Lim, W. A. Integration of multiple signals through cooperative regulation of the N-WASP-Arp2/3 complex. *Science* **290,** 801–806 (2000).

METHODS

Cells and plasmids. Wild-type *Dictyostelium discoideum* cells of the AX2 strain, obtained from the R. Kay laboratory (MRC Laboratory of Molecular Biology, UK), were used in this study. The *piaA*- and *pkbA⁻*/*pkbR1⁻* cells were described previously[37,43]. *rasC⁻*/*rasG⁻* and *amiB⁻* were obtained from DictyBase stock centre. *Gγ*- cells were obtained from the M. Ueda laboratory (Osaka University, Japan), and *pikI⁻* from the R. Kay laboratory. *pikI⁻* cells were grown on a *Klebsiella aerogenes* lawn on an SM plate, while wild-type and other gene deletion cell lines were cultured axenically in HL5 at 22°. In addition, *pkbA⁻*/*pkbR1⁻* cells were supplemented with heat-killed *Klebsiella aerogenes* during culture. Growth-stage cells were used for most experiments (except for cAMP stimulation experiments). For TIRF microscopy, starvation in suspension for 1–2 h was carried out in DB at 2×10^7 cells ml⁻¹, to reduce photosensitivity, which allowed for prolonged and frequent imaging. Cells were used within 2 months of thawing from frozen stocks.

To make membrane-anchored FKBP constructs, sequences encoding the first 150 amino acids at the N terminus of PKBR1 (denoted as 'myr'), as well as tandem FKBPs from ARGENT Regulated Heterodimerization Kit (Version 2.0), were linked with a linker sequence of 5′-AGTGCTGGTGGT-3′ and cloned into pCV5 and also pDM358. Sequences encoding mCherry, FRB, and 1–331 amino acids of Inp54p (or inactivate form Inp54p$_{D281A}$) were linked and cloned into pCV5 as well as pB18. The linker sequence between mCherry and FRB is 5′-GGAGCAAGTG GA-3′, and two repeats of 5′-AGTGCTGGTGGT-3′ were used between FRB and Inp54p. Similarly, mCherry-FRB-RasC$_{Q61L}$(4–555 bp) was constructed with 5 repeats of 5′-AGTGCTGGTGGT-3′ between FRB and RasC, as with mCherry-FRB-Rap1$_{G12V}$(1–546 bp) and mCherry-FRB-GbpD(GEF) (1–1761 bp of *GbpD*). PKBA-mCherry-FRB was constructed using two repeats of 5′-AGTGCTGGTGGT-3′ as a linker between PKBA and mCherry. Biosensors PH$_{plcδ}$-YFP, PTEN-GFP, PH$_{crac}$-YFP and j-YFP were cloned into pCV5. Conventional RBD-GFP was used in Fig. 3e and Supplementary Fig. 6, while the longer version RBD (51–220 amino acids of Raf)-YFP[55] was used in Fig. 3a to enhance expression and reduce toxicity. PH$_{crac}$-YFP/LimE-RFP in the same pDM358 vector with the due expression cassette was built using the shuttle vector pDM344. myr-FKBP-FKBP/myc-Rap1$_{S17N}$ (pDM358) was built similarly for experiments in Fig. 3d where dominant-negative Rap1 was overexpressed.

For experiments where cells overexpressed two proteins, as presented in Figs 1c–f and 3d and Supplementary Figs 1b–f, 2 and 3, and Supplementary Videos 1 and 2, the combination of pB18 and pDM358 was used. The cells were first transformed with mCherry-FRB-X in pB18 by electroporation and selected with G418 (20 μg ml⁻¹). Then the selected cells were transformed again with myr-FKBP-FKBP in pDM358 and cultured with G418 (20 μg ml⁻¹) and hygromycin (50 μg ml⁻¹).

For experiments where cells overexpressed three proteins, as presented in Figs 1b, 2, 3a–c,f, 4 and 5 and Supplementary Figs 1a, 5, 6g,h and 7 and Supplementary Videos 3–9 and 11, two alternative transformation systems were used. One is the combination of biosensor (pCV5), mCherry-FRB-X (pCV5), and myr-FKBP-FKBP (pCV5), and the cells were cultured with G418 (20 μg ml⁻¹). The other is the combination of biosensor (pCV5), mCherry-FRB-X (pCV5), and myr-FKBP-FKBP (pDM358), and the cells were cultured with both G418 (20 μg ml⁻¹) and hygromycin (50 μg ml⁻¹).

For experiments where cells overexpressed four proteins, as presented in Fig. 4c and Supplementary Video 10, FRB-Inp54p (pCV5), myr-FKBP-FKBP (pCV5) and PH$_{crac}$-YFP/LimE-RFP (pDM358) were used, and the cells were cultured with both G418 (20 μg ml⁻¹) and hygromycin (50 μg ml⁻¹).

For experiments with inducible RasC$_{Q61L}$ in Supplementary Fig. 2d,e, we used the pDM359 vector, obtained from the DictyBase stock centre. Cells were cultured in hygromycin (50 μg ml⁻¹) and RasC$_{Q61L}$ expression was induced with doxycycline (10 μg ml⁻¹) for 12 h before imaging.

Microscopy. Growth-phase cells were placed in an eight-well coverslip chamber and allowed to adhere for 10–15 min. Then the medium was replaced with 450 μl DB. To add 5 μM rapamycin in most experiments, firstly 1 μl stock (10 mM in dimethylsulfoxide (DMSO)) was diluted with 200 μl DB, and then 50 μl of the solution was added to the 450 μl in the chamber drop wise. Imaging usually started no later than 30 min after DB replacement. For the experiments presented in Fig. 3d, cells were incubated with 40 μM LY294002 or 20 μM PP242 or both for 80–100 min in DB before imaging started. For the experiments presented in Figs 3e,f and 4e–g and Supplementary Video 11, cells were treated with 5 μM latrunculin A in DB for about 30 min.

A Zeiss LSM780 single-point laser-scanning microscope (Zeiss AxioObserver with 780-Quasar confocal module; 34-channel spectral, high-sensitivity gallium-arsenide phosphide detectors, GaAsP) was used for confocal image acquisition.

Total internal reflection fluorescence (TIRF) microscopy was carried out with a Nikon Eclipse TiE microscope illuminated by an Ar laser (YFP) and diode laser (mCherry). Images were acquired by a Photometrics Evolve EMCCD camera controlled by Nikon NIS-Elements.

Phase illumination on a Zeiss Observer.Z1 inverted microscope equipped with a 20×/0.3 air objective or a 40× oil objective was used for phase image acquisition.

Image analysis. Images were analysed with ImageJ (NIH) and MATLAB (MathWorks).

Mean cytosolic intensity was measured by manually selecting the cytosolic portion of the cells (Figs 1a and 5a,b). The responses to cAMP stimulation (Fig. 5c,d and Supplementary Fig. 7) were calculated from the decrease in the mean cytosolic fluorescence. Each value point came from 1 minus the mean peak value (within 30 s after cAMP) of PH$_{crac}$ cytosolic intensity in the individual condition, and then was normalized by the response to 100 nM cAMP.

To get the ratio of membrane to cytosol intensity in Fig. 1b and Supplementary Fig. 1a, the cell image was first converted to binary after the threshold was adjusted to cover all the pixels of the cell, yielding image A. Then 'Erode' was used to generate image B and 'Erode' was applied a second time to generate image C. Image B was subtracted from image A by 'Image Calculator' to get Image D. Image D was multiplied with the original cell image to get the pixels of membrane portion. Image C was multiplied with the original cell image to get the cytosol portion. The mean intensity of the membrane portion and cytosol portion were measured and the ratio was calculated.

Cell areas in Fig. 1e were measured by using the 'Analyze Particle' function on threshold-adjusted cell images, and were normalized according to each mean cell area before rapamycin addition.

The cell outline overlays in Fig. 1d were generated using the 'Find Edges' and 'Time-Lapse Colour Coder' in ImageJ. The overlays in Fig. 2b,d,f, and Supplementary Fig. 5a,c were generated by 'Time-Lapse Colour Coder' in ImageJ. The cell outlines in Fig. 7a,c–e, and Supplementary Videos 8 and 9 were obtained manually and imposed on the images.

The ImageJ 3D Viewer plugin was used to stack the frames from videos to create the *T*-stacks in Figs 2a and 7b, as previously described[11]. The resampling factor is set to 1 to avoid blurring of activities between frames.

The kymographs presented in Figs 2–4 and Supplementary Figs 5 and 6h were created using the image processing toolbox of MATLAB (MathWorks) as previously described[11]. Colours were assigned linearly in the same fashion across all kymographs, with blue indicating the lowest intensity and red the highest.

The cell tracks presented in Fig. 1d and Supplementary Fig. 1 were created using the Gradientech Tracking Tool, by clicking the centroid of each cell in each frame (videos were acquired every 12 s).

The wave speed presented in Fig. 4d was measured in ImageJ. The TIRF micrographs were adjusted to emphasize edges of propagating waves, and then the distance between two fixed locations along the propagating direction was measured, as well as the time that the wave edge crossed these two locations. Such measurement was carried out three times for each cell, and each data point in the figure represents the averaged value. The lagging edges of the waves were measured for oscillators.

Distribution of biosensor activity sizes. The sizes of the activity patches, as presented in Figs 3e,f, 4e and Supplementary Fig. 6, were computed using a custom MATLAB script. The fluorescent images were first segmented using an adaptive threshold, followed by morphological opening (MATLAB commands: adaptthresh, imbinarize, imerode, bwareaopen, imdilate, imfill and imclearborder, were applied in that order). The round, latrunculin-treated cells were then identified using the circular Hough transform (MATLAB command: imfindcircles). The intensity around the perimeter was then computed, smoothed with a moving average filter of length three, and compared with the mean and standard deviation of the intensity of the interior region. A patch was defined as a contiguous region around the perimeter that is at least two standard deviations higher than the interior's mean. The 'activity size' was computed by calculating the fraction of the perimeter occupied by total patches.

Assignment of migratory modes. Each fraction in Fig. 1f was obtained by manually following every cell appearing in the same field (354.25 μm × 354.25 μm) in a 10-min time window. Fan-shaped cells resemble fish keratocytes, with protrusions persistently taking over one side of the cell and migrate almost in a straight line. Oscillatory cells exhibit repeatedly spreading and crunching morphologies. The rest were assigned as amoeboid mode. Based on corresponding videos, migratory modes of every cell, including the ones that migrated in or out of the field, are identified and prorated according to the time spent in the window. A rougher quantification was used for Figs 3d and 7f and Supplementary Figs 2 and 3 in which a cell was identified as a responding cell (fan-shaped or oscillatory) as long as it showed any spreading morphology in the selected time window, and in which fans and oscillators were not separated.

Automatic assignments were carried out in MATLAB (MathWorks) as detailed in Supplementary Fig. 4. Fans were defined as cells that migrated perpendicular to their long axis, oscillators as cells that displayed a large variance in area, and amoeboid cells as cells with small variance in area.

Excitability of PH$_{crac}$ to cAMP stimulation. Cells associated with Fig. 5 and Supplementary Fig. 7 were developed in suspension, by pulsing with 50–100 nM cAMP every 6 min at 2×10^7 cells ml^{-1} for about 4 h. Then, cells in 450 μl DB were plated in one 8-well chamber, and incubated with 5 μM latrunculin A for about 30 min. Confocal imaging was performed during which 50 μl cAMP solution (tenfold dilution) was added. Images were acquired every 2.5 s. Then to get rid of cAMP, all medium in this well was carefully removed, followed by immediately replenishing fresh DB media with 5 μM latrunculin A and 5 μM rapamycin. The chamber and the cells could not be perturbed to keep observing the same cells in the same field. After incubation for 10–15 min, confocal imaging was performed again with stimulation by the same concentration of cAMP. The same process was repeated using other wells of cells to get data of other concentrations of cAMP stimulation.

Cell migration assay. *amiB*$^-$ and *pikI*$^-$ chemotaxis assays were carried out using clear-view migration plates (Incucyte). Briefly, cells were seeded at a density of 4×10^3 cells in the upper chamber of the cell migration plate and allowed to chemotaxis to folic acid at the indicated concentrations in the lower chamber for 3 h. Chemotaxis was scored using Incucyte Zoom software (Essen Biosciences).

Simulation of excitable signal transduction system. The excitable network is described by three interacting states (Fig. 8a). State F is mutually inhibitory to state B and initiates a negative feedback loop through state R. The system can be described by the following three partial-differential equations:

$$\frac{\partial F}{\partial t} = D_F \nabla^2 F - (a_1 + a_2 R) F + \tilde{a}_3 \left(\frac{1}{\tilde{a}_4^2 + B^2} + U_B \right) (a_5 - F) + a_6 U_N$$

$$\frac{\partial B}{\partial t} = -b_1 B + \frac{b_2}{F}$$

$$\frac{\partial R}{\partial t} = D_R \nabla^2 R - c_1 R + c_2 (g - \varphi P) F$$

Note that if the coefficients for the equation for B are large, then we can approximate this state by its quasi-steady-state value

$$B \approx \frac{b_2}{b_1} \frac{1}{F}$$

Replacing this into the equation for F leads to the second-order system

$$\frac{\partial F}{\partial t} = D_F \nabla^2 F - (a_1 + a_2 R) F + a_3 \left(\frac{F^2}{a_4^2 + F^2} + U_B \right) (a_5 - F) + a_6 U_N$$

$$\frac{\partial R}{\partial t} = D_R \nabla^2 R - c_1 R + c_2 (g - \varphi P) F$$

where $a_3 = \tilde{a}_3/\tilde{a}_4^2$ and $a_4 = (b_2/b_1 \tilde{a}_4)$, resulting in a two-species activator–inhibitor system as previously considered[16]. Both the components in this system can diffuse spatially, with diffusion coefficients D_F and D_R, respectively. The signals U_B, U_N and P are inputs to the excitable system. They refer to the basal level of activation, the stochastic component and the polarization component, respectively (explained in more detail below). In this case there is no external stimulus[27], as we are interested in the system response to intrinsic noise. However, for the dose response—where we simulated the response to different levels of cAMP, the U_N term was replaced with the cAMP concentration. The stochastic component is modelled as a zero mean, white noise process with a controllable variance: to modulate the amount of noise in the system.

Additionally, we incorporate a polarity mechanism given by $P = Z - W$, where the individual components are implemented as local excitation, global inhibition mechanisms[27]:

$$\frac{\partial Z}{\partial t} = D_Z \nabla^2 Z - k_{-Z} Z + k_Z \sigma_{pro}$$

$$\frac{\partial W}{\partial t} = D_W \nabla^2 W - k_{-W} W + k_W \sigma_{pro}$$

For simplicity, we let D_W be sufficiently high that W is spatially independent. The polarization module is activated by signal σ_{pro}, which represents the stress from actin polymerization and is proportional to R. The complete system is shown in Supplementary Fig. 8a.

Varying the slope of the *R*-nullcline gives rise to different cell behaviours. If we fix P, set each of the partial equations to zero and solve for R as a function of F we obtain the two nullclines of the activator–inhibitor system. The parameter g determines the slope of the *R*-nullcline (Supplementary Fig. 8b). The difference between the equilibrium state and the minimum of the *F*-nullcline roughly dictates the threshold of the system, where decreasing the value of g causes a decrease in threshold and vice versa. In amoeboid cells (slope: $g_{ame} = 5.5$), if noise is sufficient to perturb the steady state across the threshold, a large excursion in the phase plane takes place before the system settles back to equilibrium (Supplementary Video 13). The contribution of the time- and spatially dependent P causes the *R*-nullcline to oscillate around the steady state as the excursions take place. It subsequently causes the threshold to lower at the front of cells and increase at the back, thus making it unlikely for the back to get excited, resulting in the cell becoming polarized in one unique direction. Fan-shaped cells manifest at a lower threshold (slope: $g_{fan} = 4.6$), with strong polarity at the front, causing the nullcline to shift across the minimum resulting in oscillations at the front (Supplementary Video 13). Reducing this slope further (slope: $g_{osc} = 2.2$) leads to oscillators as the *R*-nullcline shifts completely to the right of the minimum of F and creates an unstable equilibrium state for the whole cell, in which case, the slightest perturbation drives the system into periodic large excursions, without the system ever reaching steady state again, resulting in whole-cell expansions and contractions (Supplementary Video 13).

To see the whole spectrum of cell behaviours on one kymograph (Fig. 6g), we held the slope constant at 6 until $t = 100$, after which it was lowered exponentially so that, at $t = 600$, the slope was 2, thereby encompassing the required thresholds for amoeboid cells, fans and oscillators, and enabling us to visualize their transition. To determine the probabilities of each migratory mode at different time points (Fig. 6h), we used the random number generator in MATLAB (Mathworks) to obtain random slopes between 6 and 2, and then categorized the responses at each time point. The dose–response curve (Fig. 6i) was similarly simulated where the higher thresholds were obtained by generating random slope values between 6.5 and 5.5 (blue), and lower threshold values between 5 and 2 (red), and then normalizing the peak response to each threshold by the maximum simulated response at 100 nM cAMP.

Simulating cell morphology. To determine the effect of these changes on morphology we simulated cell behaviour using level set methods (LSM), as previously described[56]. Briefly, in the LSM the cellular boundary is defined as the zero-level set of a potential function $\varphi(x,t)$, $x \in \mathbf{R}^2$ whose evolution of the cell is described by the equation:

$$\frac{\partial \varphi(x,t)}{\partial t} = v(x,t) \cdot \nabla \varphi(x,t) = 0 \qquad (1)$$

where $v(x,t)$ describes the local velocity of the potential function. To obtain this velocity we apply different stresses on the cell and use a viscoelastic mechanical model of the cell to determine the local velocity. In our case we use:

$$\dot{x}_{mem} = -(K/D) x_{cor} + (1/D + 1/B) \sigma_{tot}$$

$$\dot{x}_{cor} = -(K/D) x_{cor} + (1/D) \sigma_{tot}$$

where σ_{tot} is the total stress applied on the cell, x_{mem} and x_{cor} are the local displacements of the membrane and cortex, respectively, and K, D and B are viscoelastic components of the cell describing the elasticity (K) and viscosity (D) of the membrane, and the viscosity of the (B) of the cytoplasm. The velocity in equation (1) is given by $v = \partial x_{mem}/\partial t$.

The total stress (σ_{tot}) acts normal to the cell boundary and incorporates surface tension ($\sigma_{ten} = \gamma \kappa(x)$, where γ is the local cortical tension and κ is the local curvature), volume conservation ($\sigma_{vol} = k_{area}(A(t) - A_0)$, where A is the surface area enclosed by the cell boundary either at time t or initially) and protrusive forces ($\sigma_{pro} = \sigma_0 R(\theta)$).

Parameters used in these simulations are provided in Supplementary Table 1. The model and all simulations are implemented using MATLAB. The PDEs for the signalling system were solved by representing the cell boundary as a one-dimensional system, discretized in space using 314 points. The two-dimensional simulations were carried out discretizing the system similarly on a 300×300 point lattice, using the same parameters as the one-dimensional system. Spatial diffusion terms, which contain the second derivatives, were approximated by central differences in space, subsequently converting the partial-differential equations to ordinary differential equations. The time step for simulation was set to 0.01 s. The solutions of the stochastic differential equations were obtained using the SDE toolbox for MATLAB[57]. After solving the concentrations of all species, we compute the protrusive force using the concentration for R and use this force to update the potential function in the LSM. The potential function is solved on a Cartesian grid with spatial discretization of 11 points per micrometre. The level set simulations were carried out using the Level Set Toolbox for MATLAB using the first forward Euler method[58].

Statistics and reproducibility. Statistical significance and *P* values were determined using the two-tailed *t*-test in Figs 5c and 7g,h, and Supplementary Figs 2c, 3c,d, 6f and 7. One-way ANOVA with *post hoc* Tukey HSD test was used in Figs 3d and 7f. Wilcoxon–Mann–Whitney rank sum test was used in Fig. 4d. Mean values ± either s.d. or s.e.m. were reported as indicated in the figure legends, except in the scatter plots of Fig. 4d where median is shown.

Representative images were presented in Figs 1a–c, 2b,d,f, 3a–c, 4a–c,e, 5a,b and 7a,c–e, and Supplementary Figs 2a,b,d, 3a,b and 6a, which have been repeated in more than 3 independent experiments.

Code availability. Computational codes are available from the corresponding author on reasonable request.

Data availability. Source data for Figs 3d and 7f–h, and Supplementary Figs 2c, 3c,d and 6f have been provided as Supplementary Table 2. All other data supporting the findings of this study are available from the corresponding author on reasonable request.

55. Bondeva, T., Balla, A., Varnai, P. & Balla, T. Structural determinants of Ras-Raf interaction analyzed in live cells. *Mol. Biol. Cell* **13,** 2323–2333 (2002).
56. Yang, L. *et al.* Modeling cellular deformations using the level set formalism. *BMC Syst. Biol.* **2,** 68 (2008).
57. Picchini, U. SDE Toolbox: Simulation and Estimation of Stochastic Differential Equations with Matlab v. 1.4.1. (2007); http://sdetoolbox.sourceforge.net
58. Mitchell, I. M. The flexible, extensible and efficient toolbox of level set methods. *J. Sci. Comput.* **35,** 300–329 (2008).
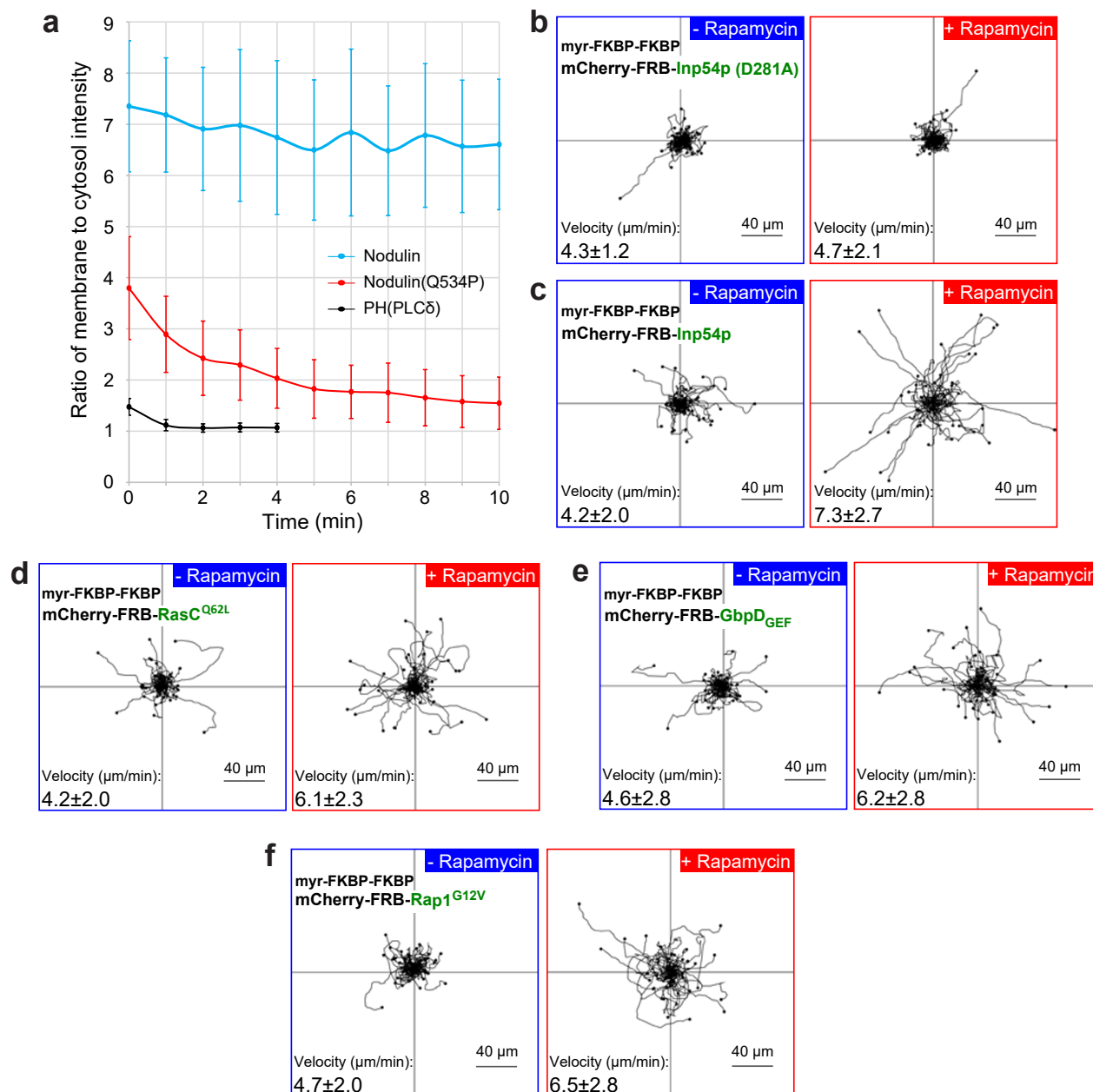
Supplementary Figure 1 Multiple acute perturbations altered cell migratory profile. (a) Ratios of membrane to cytosol intensity of PIP2 biosensors following rapamycin treatment at time 0 (mean±s.d., n=21 cells for each biosensor). "Nodulin" refers to the Nlj6-like nodulin domain of the *Arabidopsis* Sec14-nodulin protein AtSfh1[41], which has been shown to specifically bind PIP2. Nodulin^{Q534P} is a mutant with defects in self-oligomerization and thus diminished affinity for PIP2. (b-f) Centroid tracks of random cell migration before and after rapamycin addition. Cells expressed myr-FKBP-FKBP as well as mCherry-FRB-Inp54p$_{D281A}$ (b), mCherry-FRB-Inp54p (c), mCherry-FRB-RasC$_{Q62L(\Delta CAAX)}$ (d), mCherry-FRB-GbpD(GEF) (e), and mCherry-FRB-Rap1$_{G12V(\Delta CAAX)}$ (f). Rapamycin was added at time 0. Blue box, -10 to 0 min time window; Red box, 10 to 20 min time window. Tracks are reset to the same origin and n=50 cells for each, mean±s.d..
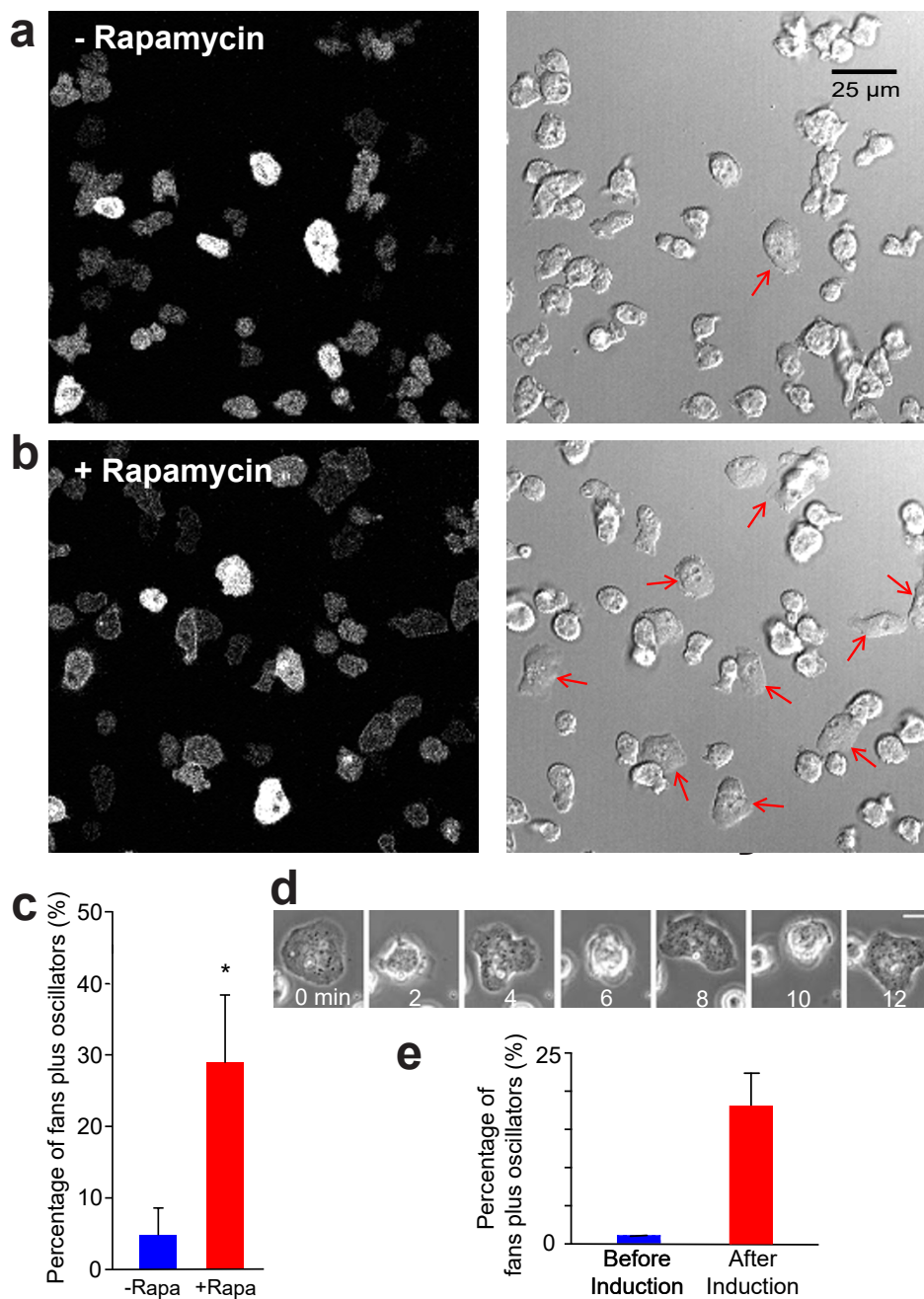
Supplementary Figure 2 Rapidly increasing RasC activity led to cell migratory modes changes. (a, b) Still images of cells expressing mCherry-FRB-RasC$_{Q62L(\Delta CAAX)}$ and myr-FKBP-FKBP before (a) and after (b) rapamycin addition in the same field. Left, confocal image of mCherry-FRB-RasC$_{Q62L(\Delta CAAX)}$. Right, bright-field image. Red arrows point to fans or the spreading phase of oscillators. (c) Percentage (mean±s.d., n=3 experiments, >500 cells in each experiment, *P=0.015, two-tailed t-test) of fan-shaped plus oscillatory cells before and after rapamycin addition (recruiting RasC$_{Q62L(\Delta CAAX)}$). Blue, 10 to 0 min before rapamycin addition; Red, 10 to 20 min after rapamycin addition. (d) Time-lapse phase-contrast images showing oscillations in induced RasC$_{Q62L}$ expressing cells. Scale bar represents 10 μm. (e) Percentage (mean±s.d., n=4 experiments, >100 cells in each experiment) of fan-shaped plus oscillatory cells before (blue) and after (red) induction of RasC$_{Q62L}$. Doxycycline was added 12 hours prior, and cells were scored over a one-hour time window before and after induction.
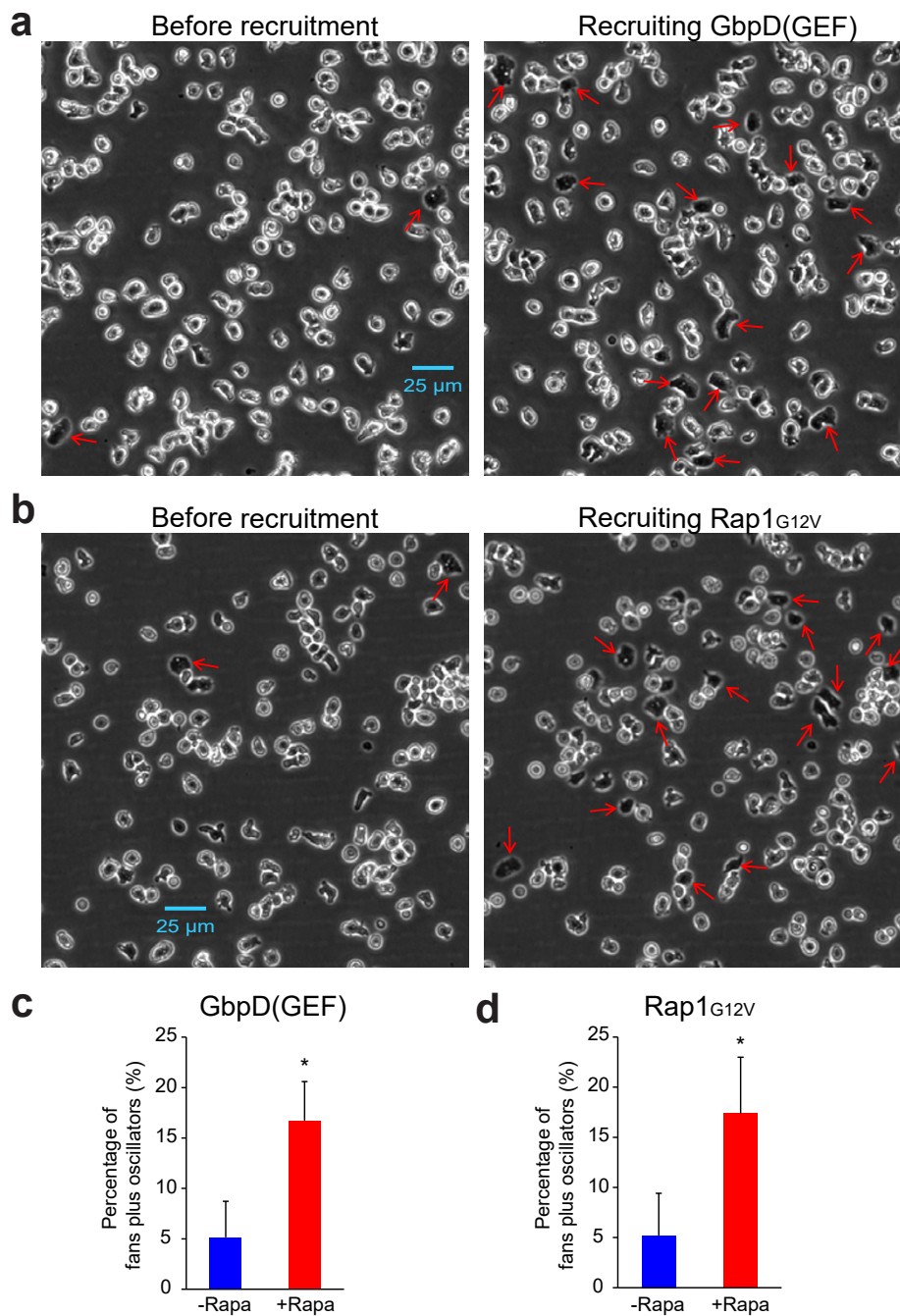
Supplementary Figure 3 Rapidly increasing Rap1-related activity led to cell migratory modes changes. (a, b) Still Phase-contrast images of cells expressing mCherry-FRB-GbpD(GEF) (a) or mCherry-FRB-Rap-$1_{G12V(\Delta CAAX)}$ (b), in addition to myr-FKBP-FKBP, before and after rapamycin addition in the same field. Red arrows point to fans or the spreading phase of oscillators, which appeared phase-dark under Phase-contrast microscopy. (c, d) Percentage (mean±s.d., n=3 experiments, >300 cells in each experiments, *P=0.019 in c and 0.04 in d, two-tailed t-test) of fan-shaped plus oscillatory cells before and after rapamycin addition, recruiting GbpD(GEF) in c and Rap1$_{G12V(\Delta CAAX)}$ in d. Blue, 10 to 0 min before rapamycin addition; Red, 10 to 20 min after rapamycin addition.
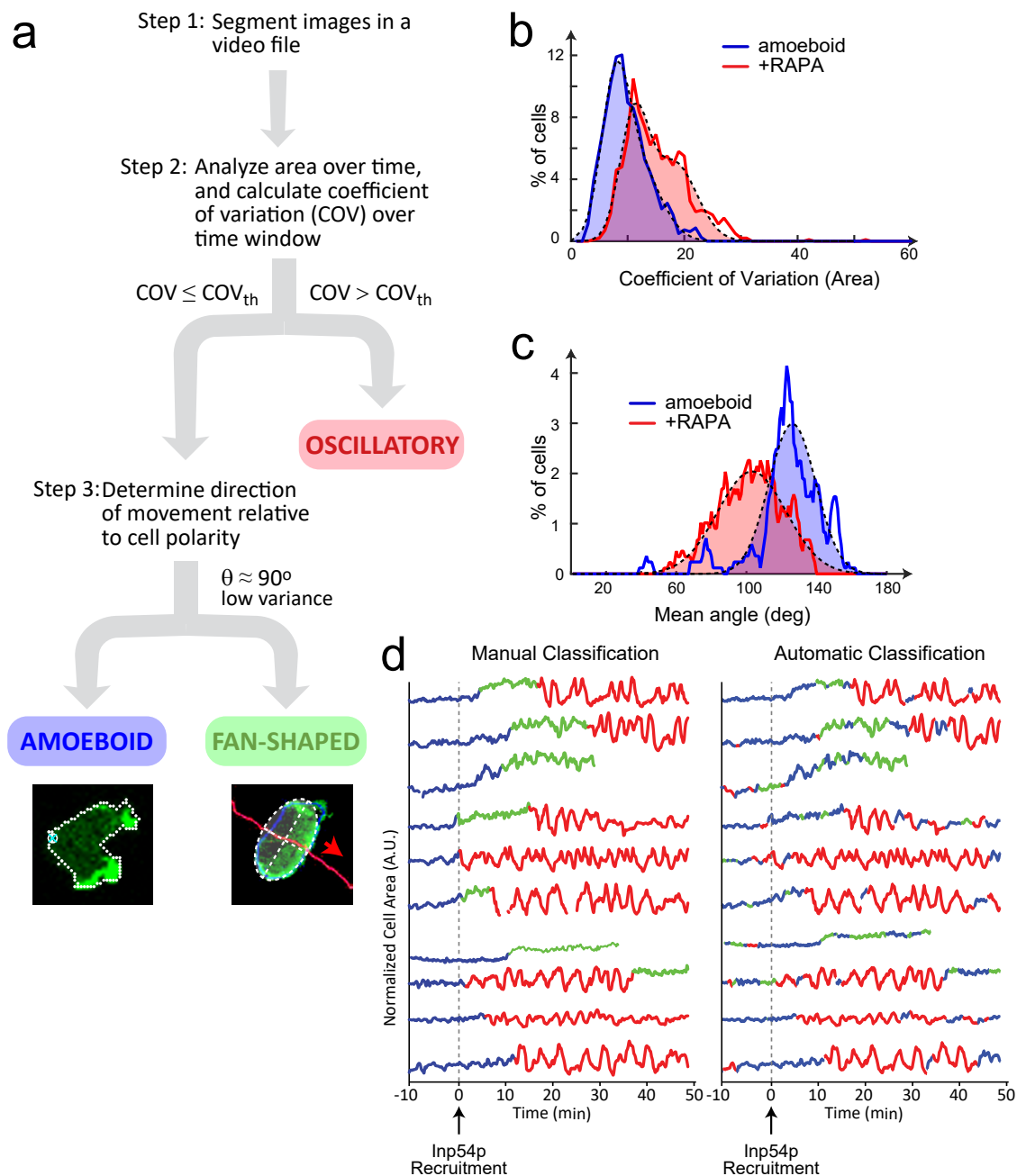
Supplementary Figure 4 Automatic classification of migratory modes. (a) Algorithm for classification of cells begins with segmentation (Step 1) which is used to determine how cell area changes over time. Cells whose coefficient of variation (COV) of area is higher than a threshold (COV_{th}=18) are deemed to be oscillatory (Step 2). Otherwise, they are classified into fan-shaped or amoeboid based on the direction of motion relative to cell polarity angle (Step 3). (b) Histograms of coefficient of variation of area (COV) for WT amoeboid cells (blue) and the population mixture after rapamycin addition (red). Data was fit by two Gaussians of varying means (8.7, 89% and 16.1, 11% for amoeba; 10.9, 27% and 16.1, 73% for rapamycin-treated cells). The COV_{th} threshold used in Step 2 was chosen based on this data. The fitted curves are shown by the dotted, shaded regions. (c) Histograms representing the mean value of Θ (from Step 3 in **a**) in cells with low variation (less than 30º) of the angle. The rapamycin-treated cells have a shift in the peak from around 130º to 100º depicting the presence of fan-shaped cells in the population. Dotted, shaded regions represent Gaussian fits (126º and 103º, respectively). (d) Comparison of the classification of cells into different migratory modes using automatic (right) versus manual inspection (left). Blue, green and red correspond to amoeboid, fan-shaped and oscillatory cells, respectively.
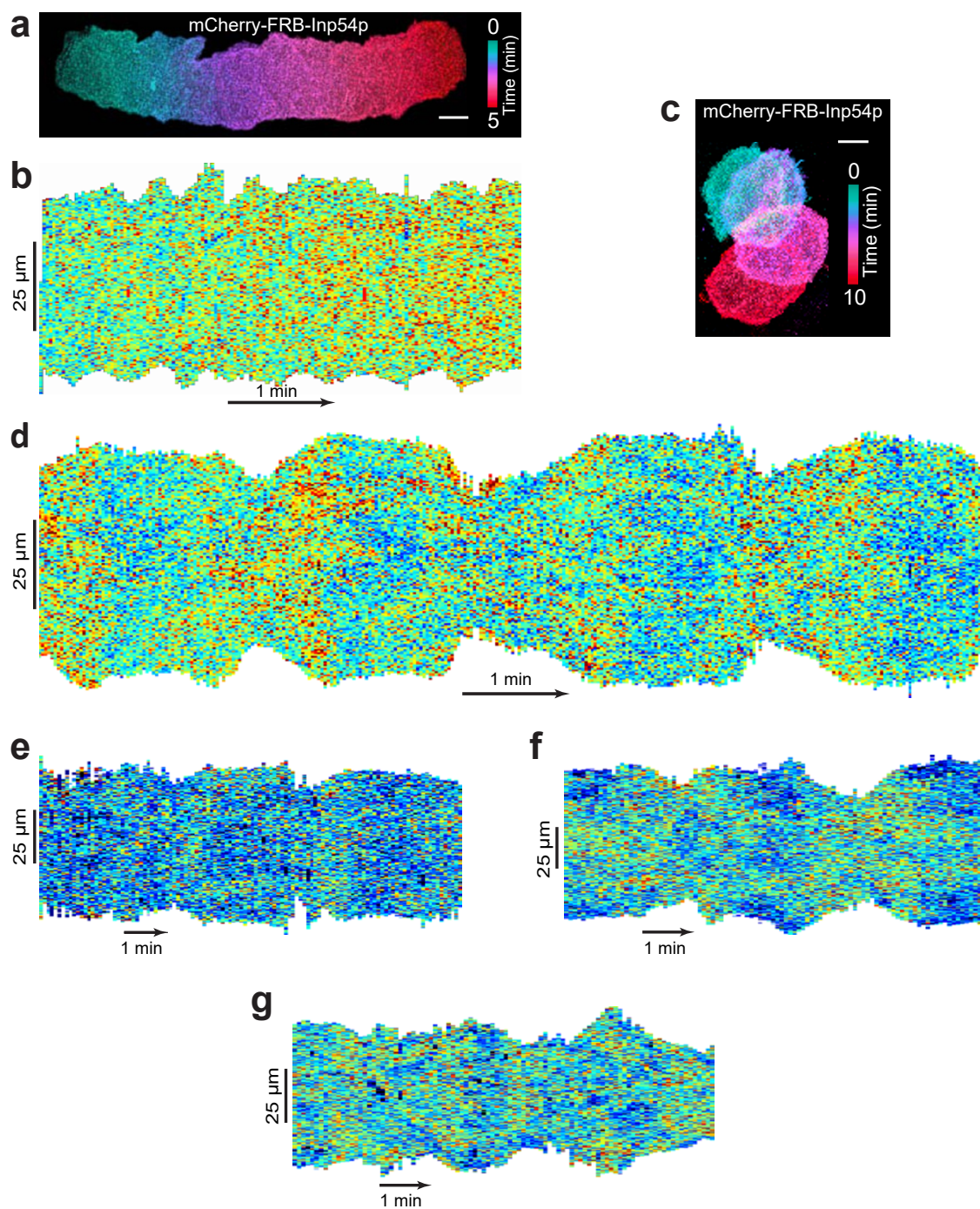
Supplementary Figure 5 Profiles of recruited mCherry-FRB-Inp54p as membrane control. (a, c) Overlays color-coded at 2 sec intervals, corresponding to Fig. 2d, f, respectively. Scale bars represent 10 μm. (b, d, e, f, g) Kymographs of membrane mCherry intensity, corresponding to Fig. 2e, 2g, 3a, 3b, and 3c, respectively.
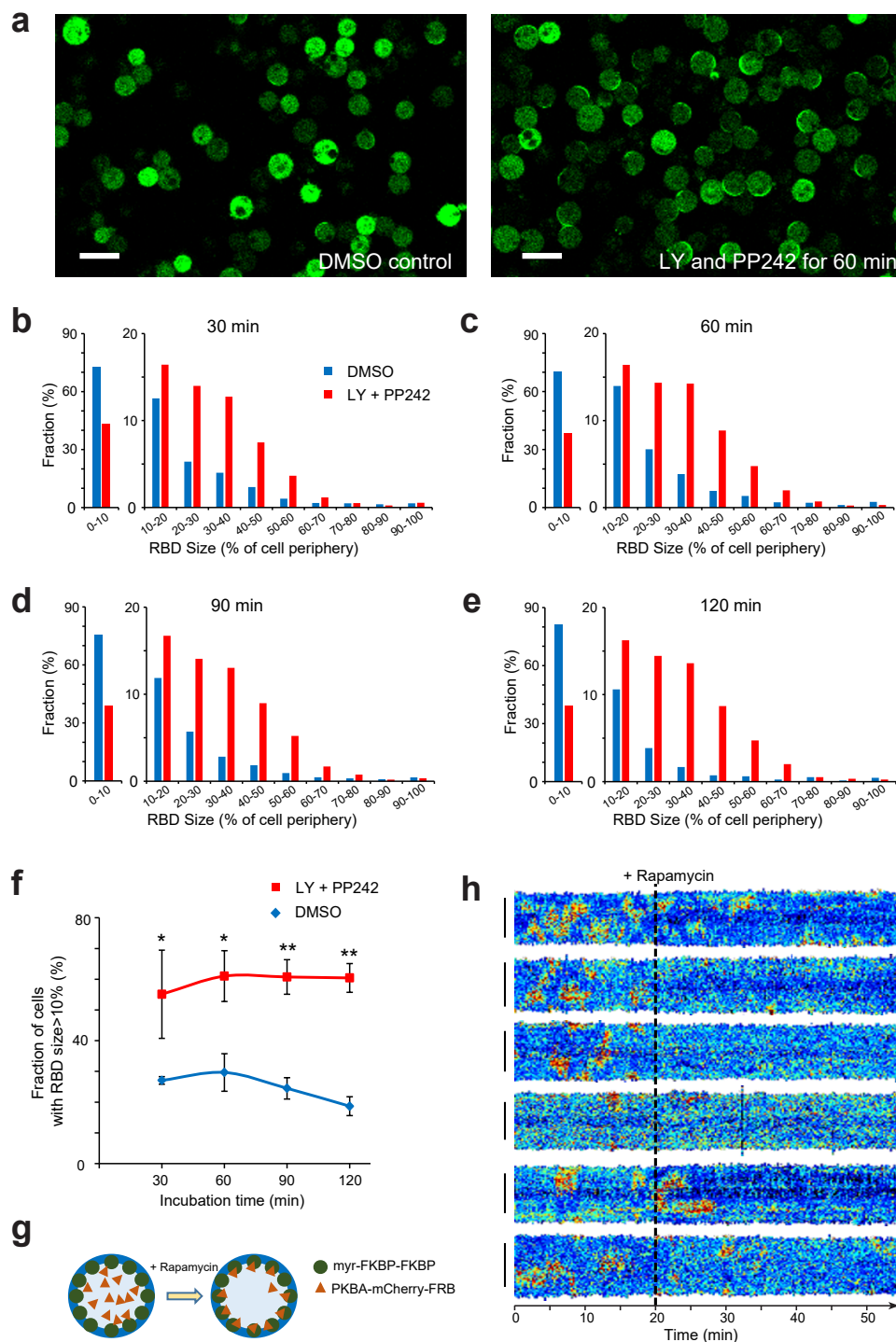
Supplementary Figure 6 PKBs negatively regulate Ras and PI3K activities. (a) Confocal images of RBD-GFP in DMSO control cells (left) and cells treated with LY294002 plus PP242 for 60 min (right). Scale bars represent 20 μm. (b-e), Distributions of different sizes of RBD-GFP activity in cells treated with DMSO (blue) and both inhibitors (red) for 30, 60, 90, and 120 min, respectively (>4500 cells from 3 independent experiments). (f) Fractions of cells with large RBD size (>10% of cell perimeter) after treatment of DMSO (blue) and both inhibitors (red) for different amount of time (mean±s.d., n=3 experiments, >1500 cells in each experiment, *P=0.028, 0.0061, **P=0.00068, 0.0002, two-tailed t-test). 5 μM LatrunculinA, 50 μM LY294002, and 20 μM PP242 were used. (g) Illustration of recruiting PKBA by the inducible dimerization system. (h) Kymographs of cortical PH_{crac}-YFP in LatrunculinA-treated cells before and after recruiting PKBA. The black dashed lines indicate rapamycin addition. Solid vertical lines on the left of each kymograph represent 20 μm.
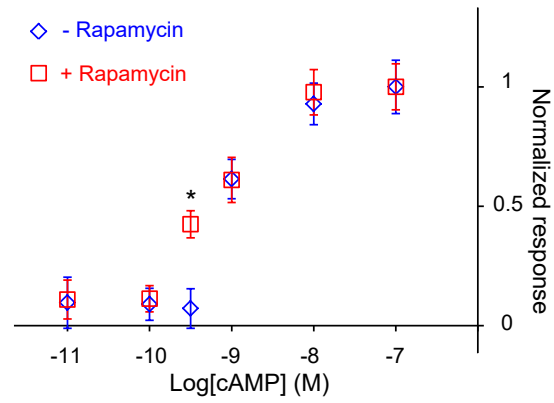
Supplementary Figure 7 Threshold for STEN activation was lowered by clamping activated RasC activities. Mean normalized responses of PH_{crac}-YFP to doses of cAMP before (blue) and after (red) recruiting $RasC_{Q62L(\Delta CAAX)}$. n=23 cells for each condition and error bars indicate standard error, $*P$=0.0017, two-tailed t-test.
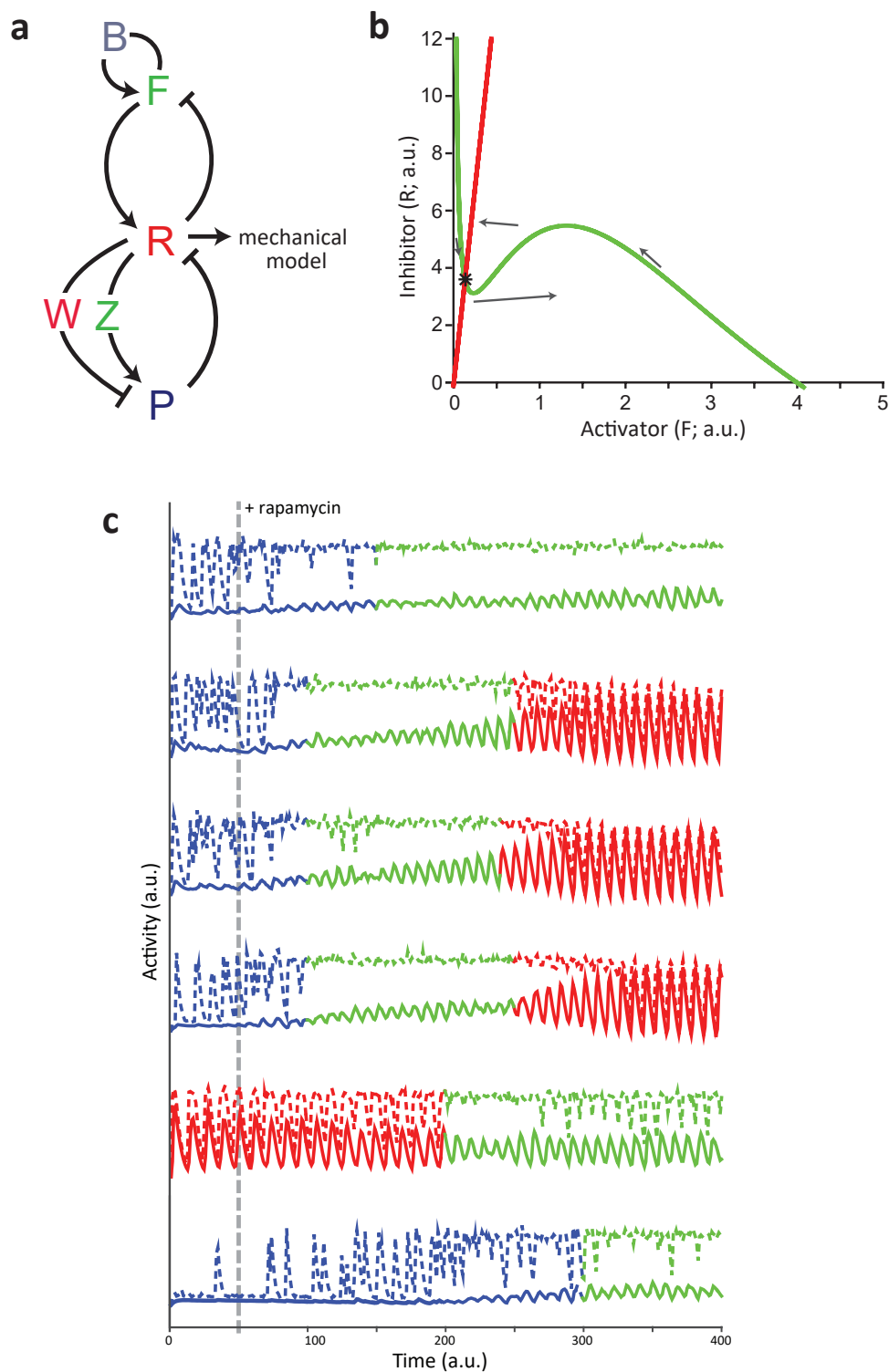
Supplementary Figure 8 Model of the excitable signal transduction network. (a) The excitable network with the polarization module. (b) Phase-plane plot of the excitable system, with the activator (F, green) and inhibitor (R, red). These plots assume that B is in quasi-steady, state and that P is constant. The black star denotes the equilibrium state of the system, while the black arrows describe the system evolution at different points in the phase plane. (c) Maximum (dashed line) and average (solid line) activities for six sample simulated cells with randomly generated thresholds. The grey line at 50 time units depicts the simulated addition of rapamycin, after which the threshold is gradually lowered. Based on the changes in the activity plots, the response was categorized as amoeboid (blue), fan-shaped (green) or oscillatory (red).

Supplementary Table Legends
Supplementary Table 1 Model parameter values for simulation of excitable network.

Supplementary Table 2 Source data for Fig 3d, 7f-h, and Supplementary Fig 2c, 3c,d, 6f.

Supplementary Video Legends
Supplementary Video 1 Time-lapse confocal videos of mCherry in cells before and after recruiting Inp54p$_{D281A}$ (left) and Inp54p (right), corresponding to Fig. 1. Cells on the left expressed myr-FKBP-FKBP and mCherry-FRB-Inp54p$_{D281A}$, and cells on the right expressed myr-FKBP-FKBP and mCherry-FRB-Inp54p. Rapamycin was added at time 10 min. Scale bars represent 20 μm. Images were acquired every 12 sec and the videos are shown at 25 frame/sec.

Supplementary Video 2 Time-lapse phase video of cells before and after recruiting Inp54p, corresponding to Fig. 1c. Cells expressed myr-FKBP-FKBP and mCherry-FRB-Inp54p. Rapamycin was added at time 6 min. Examples of amoeboid-to-fan-shaped and amoeboid-to-oscillatory transitions were outlined, with blue, green, and red representing amoeboid, fan-shaped, and oscillatory, respectively. Scale bar represents 20 μm. Images were acquired every 12 sec and the video is shown at 20 frame/sec.

Supplementary Video 3 Time-lapse confocal videos of LimE-YFP in cells before and after recruiting Inp54p$_{D281A}$ (left) and Inp54p (right), corresponding to Fig. 2a. The cells were aligned to the same centroid. Three-dimensional kymographs are shown below each video. Rapamycin was added at time 10 min. Scale bars represent 5 μm. Images were acquired every 12 sec and the videos are shown at 15 frame/sec.

Supplementary Video 4 Time-lapse confocal videos of LimE-YFP in an amoeboid (top left), fan-shaped (right), and oscillatory (bottom left) cell, corresponding to Fig. 2b-h. Scale bars represent 5 μm. Images were acquired every 2 sec and the videos are shown at 15 frame/sec.

Supplementary Video 5 Time-lapse confocal videos of LimE-YFP in cells before and after recruiting RasC$_{Q62L(\triangle CAAX)}$ (left), GbpD(GEF) (middle), and Rap-1$_{G12V(\triangle CAAX)}$ (right). Rapamycin was added at time 5 min. Scale bars represent 20 μm. Images were acquired every 15 sec and the videos are shown at 15 frame/sec.

Supplementary Video 6 Time-lapse confocal videos of RBD-YFP (left), PH$_{crac}$-YFP (middle), and PTEN-GFP (right) in oscillatory cells, corresponding to Fig.3a-c. Scale bars represent 10 μm. Images were acquired every 5 sec and the videos are shown at 15 frame/sec.

Supplementary Video 7 Time-lapse confocal videos of LimE-YFP in cells coexpressing myr-FKBP-FKBP and mCherry-FRB-Inp54p, where 5μM rapamycin and 1mM cycloheximide were added at time 4:45 min. Scale bars represent 20 μm. Images were acquired every 15 sec and the videos are shown at 20 frame/sec.

Supplementary Video 8 Time-lapse TIRF videos of PH$_{crac}$-YFP in an amoeboid (left), fan-shaped (middle), and oscillatory (right) cell. These videos correspond to Fig. 4a. Cell outlines were imposed based on videos of mCherry-FRB-Inp54p concurrently. Scale bar represents 5 μm. Images were acquired every 15 sec and the videos are shown at 6 frame/sec.

Supplementary Video 9 Time-lapse TIRF videos of LimE-YFP in an amoeboid (top left), fan-shaped (right), and oscillatory (bottom left) cell. These videos correspond to Fig. 4b. Cell outlines were imposed based on videos of mCherry-FRB-Inp54p concurrently. Scale bar represents 5 μm. Images were acquired every 10 sec and the videos are shown at 8 frame/sec.

Supplementary Video 10 Time-lapse confocal videos, focused on the bottom plane, of LimE-RFP (left) and PH$_{crac}$-YFP (right) in an oscillatory cell. These videos correspond to Fig. 4c. Scale bar represents 5 μm. Images were acquired every 2 sec and the videos are shown at 16 frame/sec.

Supplementary Video 11 Time-lapse confocal videos of mCherry-FRB-Inp54p (left) and PH$_{crac}$-YFP (right) in cells treated with 5 μM LatrunculinA before and after addition of rapamycin at time 10 min, corresponding to Fig. 4e, f. Scale bars represent 20 μm. Images were acquired every 15 sec and the videos are shown at 20 frame/sec.

Supplementary Video 12 Two-dimensional simulations on a periodic grid showing waves of activity propagating outward and collapsing corresponding to Fig. 6a-c, with the green and red denoting the activator and inhibitor, respectively. The bottom panel shows how the slope of the R-nullcline is gradually lowered thereby decreasing the threshold for activation.

Supplementary Video 13 Level set simulations of the three different migratory modes corresponding to Fig. 6d-f. The video also shows the trajectory of the equilibrium state on the phase plane, for the three different thresholds, where the particular state shown reflects the behavior of one of the points on the cell membrane, indicated by the moving white bar on the kymograph. Scale bars represent 10 μm.

Supplementary Video 14 Level set simulations of the transitions between the amoeboid to fan-shaped and the fan-shaped to oscillatory states corresponding to Fig. 6g. The transitions are simulated with a constant threshold up to the black line, after which the threshold is gradually lowered, with the red line indicating the progress in time. The transition from amoeboid to fan-shaped is demarcated by the shift in activity from a fluctuating to a constant maxima, while the transition from fan-shaped to oscillatory occurs when the maxima shifts back to a periodic cycle. Scale bars represent 10 μm.

Supplementary Video 15 Time-lapse phase-contrast video of *pikI-* cells before (left) and after (right) 40 μM LY294002 treatment, corresponding to Fig. 7a, c. Scale bar represents 10 μm. Images were acquired every 12 sec and the video is shown at 7 frame/sec.

Supplementary Video 16 Time-lapse phase-contrast video of *amiB-* cells in the same field before and after 30 μM LY294002 treatment, corresponding to Fig. 7d-f. Scale bar represents 50 μm. Images were acquired every minute and the video is shown at 7 frame/sec.